

Self-Induced Transparency in Atomic Rubidium

R. E. Slusher and H. M. Gibbs

Bell Laboratories, Murray Hill, New Jersey 07974

(Received 3 August 1971)

Self-induced transparency has been studied in detail experimentally for a simple two-level atomic absorption. A Hg II laser pulse is used at resonance with the D_1 line of Rb. This system eliminates many previous experimental problems such as nonuniform wave fronts and degenerate off-resonant absorbers. Nonlinear transmission, pulse delays, pulse breakup, peak amplification, incoherent-decay effects, off-resonance effects, and focusing effects have been observed. Quantitative comparison with theory is obtained by computer solutions which include the incoherent decay and optical-pulse shapes of the Hg-Rb system. Good agreement is obtained with the theory of McCall and Hahn. Pulse compression by an order of magnitude is obtained by focusing in the resonant absorber. The theory predicting preferred pulse widths and velocities proposed by Davidovich and Eberly is discussed and found inappropriate for the Hg-Rb and other similar systems.

I. INTRODUCTION

This article describes a detailed experimental investigation¹ of the propagation of a coherent optical pulse in a resonant absorber in the self-induced transparency² (SIT) region. These experiments use the coincidence of a Hg II laser with a simple atomic absorption in Rb(5s-5p) which provides the first system free from complications in both optical pulse (coherent, no chirping, uniform wave front, etc.) and absorber (two levels, uniform gas, no degeneracy). We investigate the following aspects of self-induced transparency: (a) nonlinear transmission, (b) pulse delays, (c) pulse breakup and peak amplification, (d) incoherent-decay effects (T_1 and T_2), (e) SIT off resonance, and (f) SIT with focused pulses. It is found that considerable attention must be given to experimental conditions such as chirping and uniformity of the wave front. However, if these effects are well understood, the simultaneous solutions of Maxwell's and Schrödinger's equations² are in excellent agreement with the experiments.

The self-induced transparency effects observed in the laboratory are quite dramatic. An optical pulse at low intensity incident on a resonant absorber is normally absorbed according to Beer's law,

$$I(L) = I_0 e^{-\alpha L}, \quad (1)$$

where I_0 is the incident intensity, α is the absorption constant, and L is the length of the absorber. αL is typically > 5 for a SIT experiment, so that low-intensity pulses are almost completely absorbed. Suddenly, as I_0 is increased, the pulse propagates through the absorber as if it were transparent, but the pulse remains in the absorber much longer ($\sim \times 10-10^4$) than required by its low-intensity velocity (c/η , where η is the index of refraction). This striking behavior has been shown for a

number of systems. The first was a ruby laser pulse incident on a liquid-helium-cooled ruby absorber.² It has also been observed in gases using CO₂ laser pulses absorbed by various SF₆ transitions near 10.6 μ .³⁻⁶ Dye laser pulses tuned to an atomic potassium resonance⁷ have also shown indications of SIT. Even acoustic pulses resonant with paramagnetic centers in solids⁸ have demonstrated SIT. However, all these experiments have unknown or uncontrolled parameters (to be discussed in Sec. II C) which make quantitative comparison with theory difficult or impossible. In contrast, this article describes results in a system that can be compared directly with the theory. In addition to a quantitative check of the theory, several new features of SIT are demonstrated including off-resonance effects, pulse compression by focusing in the absorber, breakup of the incident pulse into pulse chains, and amplification of the peak intensity of the pulse.

In addition to the experimental results, several aspects of the theory are studied in detail. The effects of incoherent relaxation by spontaneous decay of atomic levels is included into the theory. Computer solutions including incoherent decay and levels other than the resonant pair are discussed in detail. Computer solutions are important in SIT since analytical solutions and approximations have been obtained only in very limited regions. Finally, Davidovich and Eberly⁹ have questioned the theoretical approximations commonly made. They have suggested a more nearly complete solution which predicts that pulses propagating in the absorber should attain a velocity of $\frac{1}{3}c$ and a preferred pulse length. The applicability of these predictions to the Hg-Rb system and other realizable systems is discussed. It is concluded that the Davidovich-Eberly solutions do not apply in most systems studied to date.

The theory of SIT as it applies to the Hg-Rb system is discussed in Sec. II along with computer solutions which can be compared directly with the experiment. Section III presents the details of experimental apparatus for the Hg laser and Rb absorber. Section IV is a summary of the results to date including off-resonance and focusing experiments. Finally, Sec. V is a summary of the results and some suggestions for future experiments.

II. THEORY

A. Vector Model and Coupled Wave-Particle Equations

For the atomic transition in Rb investigated in this article, the vector model used to discuss SIT is particularly simple. The Rb atoms are noninteracting (in a vapor, $n \approx 10^{11} \text{ cm}^{-3}$) and are in the ground $5s$ state prior to optical excitation (see Fig. 1). This initial state is nondegenerate in a magnetic field (see Fig. 9) and for N atoms the energy of the system is $-\frac{1}{2} N\hbar\omega_0$. Now consider the effect of an applied resonant optical pulse with electric field,

$$\vec{E}(z, t) = \mathcal{E}(z, t) \left\{ \hat{x} \cos[\omega t - kz - \Phi(z)] - \hat{y} \sin[\omega t - kz - \Phi(z)] \right\}, \quad (2)$$

where $\mathcal{E}(z, t)$ is the pulse envelope, x, y , and z are spatial coordinates, $\Phi(z)$ is the phase, ω is the optical frequency, and k is the wave vector. A circularly polarized wave is chosen here since the Rb transition absorbs only one sense of circular polarization when \vec{k} is parallel to the applied magnetic field. Thermal motion Doppler-broadens the atomic transitions so that the radiation excites a fraction of the Rb dipoles proportional to the reciprocal width of the pulse envelope. However, first consider only those atoms moving perpendicular to \vec{k} whose transition frequencies ω_0 exactly match ω . Then \vec{E} causes the atomic wave function to evolve from the symmetric s state $|b\rangle$ to a superposition $(|a\rangle + |b\rangle)/\sqrt{2}$, where the system has a real optical-frequency dipole, and then to the excited state $|a\rangle$. This process takes place coherently and the energy given to the atom is coherently reradiated back into the electromagnetic field as the atom is driven back to the ground state. A pulse which drives the system from $|b\rangle$ to $|a\rangle$ and back to $|b\rangle$ is called a 2π pulse, because its area, defined by

$$A(z) = (2p/\hbar) \int_{-\infty}^{+\infty} \mathcal{E}(z, t) dt, \quad (3)$$

where the transition dipole is $p = e|\langle a|\vec{r}|b\rangle|$, is 2π . In a frame rotating at ω , \mathcal{E} appears stationary, and the induced dipole caused by the superposition of s and p states appears at 90° to \mathcal{E} . A vector \vec{P} can be defined² as

$$\vec{P} = u\hat{u}_0 + v\hat{v}_0 - (W\kappa/\omega)\hat{w}_0, \quad (4)$$

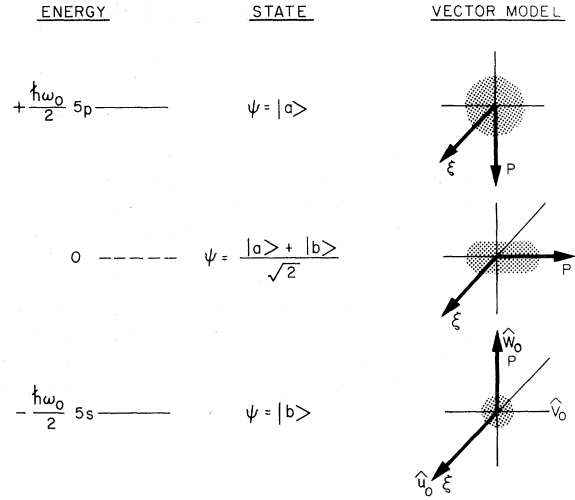


FIG. 1. Energy levels, states, and vector model for SIT for the two-level Rb atom.

where

$$\kappa = 2p/\hbar, \quad W = \frac{1}{2} N\hbar\omega_0 \langle \sigma_x \rangle,$$

$$u + iv = \frac{1}{2} Np \langle \sigma_x + i\sigma_y \rangle,$$

N is the number of atoms, and $\langle \sigma \rangle$ indicates the expectation value of a Pauli matrix. It has been shown² that \vec{P} rotates about \mathcal{E} in the rotating frame as shown in Fig. 1. In this case $A(z)$ is the angle through which \vec{P} rotates. If \mathcal{E} is off resonance by $\Delta\omega = \omega_0 - \omega$, the equation of motion for \vec{P} is

$$\dot{\vec{P}} = \vec{P} \times [\hat{u}_0 \kappa \mathcal{E}(z, t) + \hat{w}_0 \Delta\omega], \quad (5)$$

which follows directly from Schrödinger's equation and is commonly called the Bloch equation. \vec{P} is also related to \mathcal{E} by Maxwell's equation

$$\frac{\partial^2 E_+(z, t)}{\partial z^2} - \frac{\eta^2}{c^2} \frac{\partial^2 E_+(z, t)}{\partial t^2} = \frac{4\pi}{c^2} \frac{\partial^2 P_+(z, t)}{\partial t^2}, \quad (6)$$

where

$$P_+(z, t) = \int_{-\infty}^{+\infty} g(\Delta\omega) [u(\Delta\omega, z, t) + iv(\Delta\omega, z, t)] \times e^{i[\omega t - kz - \Phi(z)]} d(\Delta\omega) \quad (7)$$

and

$$E_+(z, t) = \mathcal{E}(z, t) e^{i[\omega t - kz - \Phi(z)]}. \quad (8)$$

The spectral distribution of absorbers is given by $g(\Delta\omega)$ with normalization

$$\int_{-\infty}^{\infty} g(\Delta\omega) d(\Delta\omega) = 1.$$

Equation (6) can be written as two scalar equations using the usually valid assumption that $\ddot{u} \ll \omega^2 u$ and $\ddot{v} \ll \omega^2 v$:

$$\frac{\partial \mathcal{G}}{\partial z} + \frac{1}{c} \frac{\partial \mathcal{G}}{\partial t} = -\frac{2\pi\omega}{c} \int_{-\infty}^{+\infty} g(\Delta\omega) \left(v - \frac{2\dot{u}}{\omega} \right) d(\Delta\omega) \quad (9)$$

and

$$\begin{aligned} \frac{\partial^2 \mathcal{G}}{\partial z^2} - \frac{1}{c^2} \frac{\partial^2 \mathcal{G}}{\partial t^2} - 2k \frac{\partial \Phi(z)}{\partial z} \mathcal{G} \\ = -\frac{4\pi\omega^2}{c^2} \int_{-\infty}^{+\infty} g(\Delta\omega) \left(u + \frac{2\dot{v}}{\omega} \right) d(\Delta\omega), \end{aligned} \quad (10)$$

with $\eta = 1$. It has been assumed that $\partial\Phi/\partial t = 0$, i.e., that the optical pulse is unchirped. In the experiments discussed in this article, these further simplifying approximations used by McCall and Hahn can be made: (i) The \dot{u} term is dropped in Eq. (9), and (ii) the second-order Eq. (10) is ignored altogether. Davidovich and Eberly⁹ have obtained analytic solutions for Eqs. (9) and (10) as they stand coupled with Bloch's equations, which differ significantly from the results predicted by McCall and Hahn; their analysis is inappropriate for the pulse lengths in the present experiments (see Appendix A).

One must now solve Maxwell's [Eq. (9)] and Bloch's [Eq. (5)] equations simultaneously. An analytic solution exists for $A = 2\pi$, i.e.,

$$\mathcal{G}(z, t) = \frac{2}{\kappa\tau} \operatorname{sech} \left[\frac{1}{\tau} \left(t - \frac{z}{V} \right) \right], \quad (11)$$

where V is the propagating velocity and τ is the characteristic pulse width.² Substitution back into the original equation shows that a pulse of the form of Eq. (11) is delayed in the medium by a time

$$\tau_D = \frac{1}{2} \alpha L \tau. \quad (12)$$

An inhomogeneous linewidth $1/T_2^*$ has been assumed such that $\tau \gg T_2^*$, thus assuring the same α for all Fourier components of the pulse. It is also assumed that $\alpha\tau \gg 1/c$. Both of these assumptions are valid for the Hg-Rb system. For the experiments described here $\alpha L \approx 5$, $\tau \approx 2$ nsec, and $L = 1$ mm. Thus $\tau_D \approx 5$ nsec, which means that the pulse moves through the absorber very slowly ($V \sim c/1500$). Yet the pulse is stable and propagates without attenuation since energy absorbed by the atoms is coherently reradiated back into the electromagnetic field. For actual experiments, a computer solution of the coupled Maxwell-Bloch equations is required since the input pulse is not sech in shape or 2π in area (see Sec. II B).

Before discussing the complete computer solutions, an important insight into requirements for the experiment can be gained by using a simpler approach suggested by McCall and Hahn.^{2c} This approach uses the area [Eq. (3)] and energy [Eq. (15)] to characterize the pulse. The area theorem [Ref. 2b, Eq. (36)] gives

$$\frac{dA(z)}{dz} = -\frac{\alpha}{2} \sin A(z), \quad (13)$$

and the pulse energy evolves as

$$\frac{dT(z)}{dz} = -\alpha TF(A, T, \text{pulse shape}), \quad (14)$$

where

$$T(z) = (c/4\pi) \int_{-\infty}^{+\infty} \mathcal{G}(z, t)^2 dt \quad (15)$$

is the pulse energy per unit area. A good approximation for many pulse shapes [Ref. 2c, Eq. (26) and Ref. 2b, Fig. 2] is

$$F(A) = 2(1 - \cos A)/A^2 \quad (16)$$

for $A < 3\pi$. The general solution of Eq. (13) is

$$A(z) = 2 \tan^{-1} \left[e^{-\alpha z/2} \tan \frac{1}{2} A(0) \right]. \quad (17)$$

Equations (14), (16), and (17) are simple to solve simultaneously on a computer. Figure 2(a) shows the ratio of output to input energy as a function of $A(0)$ and $T(0)$. Clearly demonstrated in this figure is the sudden onset of transparency near $A = \pi$. For Fig. 2(a) it was assumed that $\mathcal{G}(0)$ was uniform in the x - y plane. This condition is obtained experimentally only in a limited spatial region since the optical pulse always has a finite transverse dimension. For example, one often uses the Gaussian transverse profile of the TEM₀₀ mode of a laser cavity:

$$\mathcal{G}(r, z=0) = \mathcal{G}(0, 0) e^{-r^2/w^2}, \quad (18)$$

where r is the radius of the beam and w is its width. Figure 2(b) shows the computed energy ratio vs $A(0, 0)$ integrated over a Gaussian intensity profile. This shows that it is important experimentally to aperture the detector so that only the uniform region [$\mathcal{G}(r, L) \approx \mathcal{G}(0, L)$] is observed if direct comparison is to be made with the uniform plane-wave theory. Actually the experimental ratios predicted by more exact computer solutions (see Sec. II B) lie along the dashed curve in Fig. 2(c) because of pulse reshaping [Eq. (16) is not exact] and spontaneous (incoherent) decay from the Rb excited state.

In addition to coherent changes of state caused by the driving field \vec{E} , the Rb atoms decay incoherently from the excited state to two ground states (see Fig. 9). This incoherent decay modifies the pulse propagation. In particular, the 2π pulse will gradually broaden in time and lose energy and area until it falls below $A = \pi$, after which it decays rapidly to the linear absorption region where Beer's law applies [Eq. (1)].

Since the Rb decay times to the ground levels are 42 and 84 nsec and the pulse widths were 5–10 nsec, these decay mechanisms are not negligible and must be included in the theory. In Appendix B we show that the effective Bloch equations are

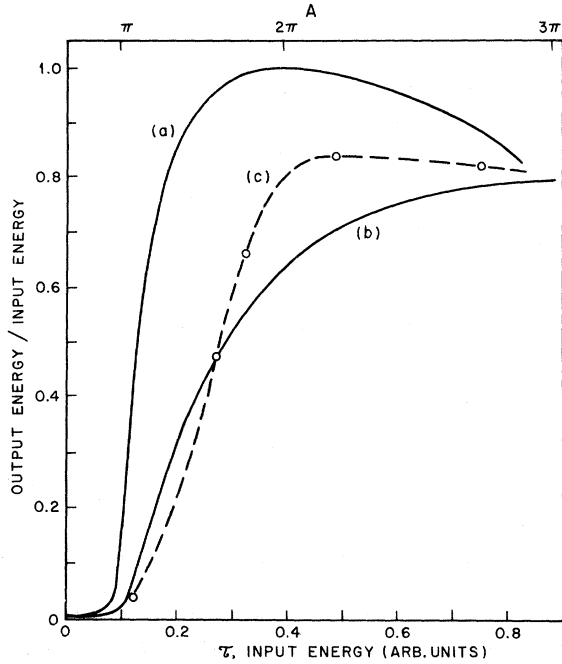


FIG. 2. Computer solutions for the output-input energy ratio of SIT pulses as a function of input energy and area; (a) assumes uniform plane wave and no losses, (b) Gaussian profile plane wave with no losses, (c) experimental pulse shapes, T_1 and T_2' losses for Rb, and uniform plane wave. All curves assume $\alpha L = 5$. Points on (c) are the only computed points; (a) and (b) used closely spaced input areas because of simplicity of program.

$$\dot{u} = v\Delta\omega - u/T_2', \quad (19)$$

$$\dot{v} = -u\Delta\omega - \kappa^2 \mathcal{E} W / \omega - v/T_2', \quad (20)$$

$$\dot{W} = v\mathcal{E}\omega - (x + W)/T_1, \quad (21)$$

$$\dot{x} = -(2/T_2' - 1/T_1)(x + W), \quad (22)$$

where

$$x = \frac{1}{2} N \hbar \omega_0 \langle I \rangle \quad (23)$$

and I is the unity matrix for the two-level system being excited. Note that $N \langle I \rangle$, the total number of atoms in the two-level system, decreases as atoms decay from the resonant two-level system to the third level. Equation (22) describes this loss of atoms by spontaneous decay. The decay rates for Rb (see Appendix B) are

$$\frac{1}{T_1} = \frac{1}{2\tau_{ac}} + \frac{1}{\tau_{ab}} = (33.6 \text{ nsec})^{-1}, \quad (24)$$

$$\frac{1}{T_2'} = \frac{1}{2\tau_{ac}} + \frac{1}{2\tau_{ab}} = (56 \text{ nsec})^{-1}, \quad (25)$$

where τ_{ab} and τ_{ac} are the decay constants from level $|a\rangle$ to levels $|b\rangle$ and $|c\rangle$ (note that if $\tau_{ac} \rightarrow \infty$, then

$T_2' = 2T_1$, as expected for a pure two-level system). We have neglected radiation trapping effects which were estimated to be small for the densities used in these experiments.

B. Computer Solutions

The input pulse envelope for real experiments, $\mathcal{E}(z, t)$ (which is rarely a simply expressed function of time), reshapes in the resonant medium and loses energy until the stable sech pulses are attained. Computer solutions seem to be the only way to make direct comparisons with theory. For Rb with pulse lengths of $\approx 1-10$ nsec, a good theoretical approximation is Eq. (9) (dropping the $2\dot{u}/\omega$ term) and Eqs. (21)–(24). During each time increment dt sufficiently short so that $\mathcal{E}(z, t)$ is nearly constant, one can assume \mathcal{E} constant and the incoherent relaxation terms zero. In this limit one can solve analytically for u , v , and W , i. e.,

$$u(t, \Delta\omega) = u_1 \{ [\kappa^2 \mathcal{E}^2 + (\Delta\omega)^2 \cos Ct] / C^2 \} \\ + (v_1 \Delta\omega \sin Ct) / C + W_1 (\kappa^2 \Delta\omega \mathcal{E} / \omega C^2) (\cos Ct - 1), \quad (26)$$

$$v(t, \Delta\omega) = v_1 \cos Ct - [(u_1 \Delta\omega + \kappa^2 \mathcal{E} W_1 / \omega) \sin Ct] / C, \quad (27)$$

$$W(t, \Delta\omega) = u_1 (\omega \mathcal{E} \Delta\omega / C^2) (\cos Ct - 1) \\ + v_1 (\omega \mathcal{E} / C) \sin Ct + W_1 \{ [(\Delta\omega)^2 + \kappa^2 \mathcal{E}^2 \cos Ct] / C^2 \}, \quad (28)$$

where

$$C = [(\Delta\omega)^2 + \kappa^2 \mathcal{E}^2]^{1/2}. \quad (29)$$

The relaxation terms of Eqs. (19)–(22) can now be included by assuming u_1 , v_1 , and W_1 are slowly varying functions of time during dt . The values of $u_1(dt)$, $v_1(dt)$, and $W_1(dt)$ were computed at the end of dt . The values used in the Eqs. (26)–(28) were the averaged values of the coefficients u_1 , v_1 , and W_1 over the interval dt . Next $v(t, \Delta\omega)$ is summed over $\Delta\omega$ in order to calculate a new value of $\mathcal{E}(t)$ from Eq. (9). The increments in $\Delta\omega$ must be carefully chosen since the full range of the Fourier transform of $\mathcal{E}(t)$ must be spanned. Computer solutions shown here used fifty $\Delta\omega$ increments each equal to $0.4/\tau_R$, where τ_R is the rise time of the optical-pulse envelope (typically 5 nsec). Because of the limit in $\Delta\omega$ integration there are oscillations expected with a period $\tau_0 \approx \pi/\Delta\omega_{\max}$. This period should be as small as possible for accurate determination of pulse shapes. The inhomogeneous Doppler shape $g(\Delta\omega)$ must also be included since for Rb⁸⁷ the inverse Doppler width is ≈ 0.8 nsec.

Proceeding as described above, computer solutions were used to predict the pulse shapes expected for the Rb⁸⁷ absorber. The experimental input pulse shapes were used with $dt = 0.2-0.5$ nsec. The com-

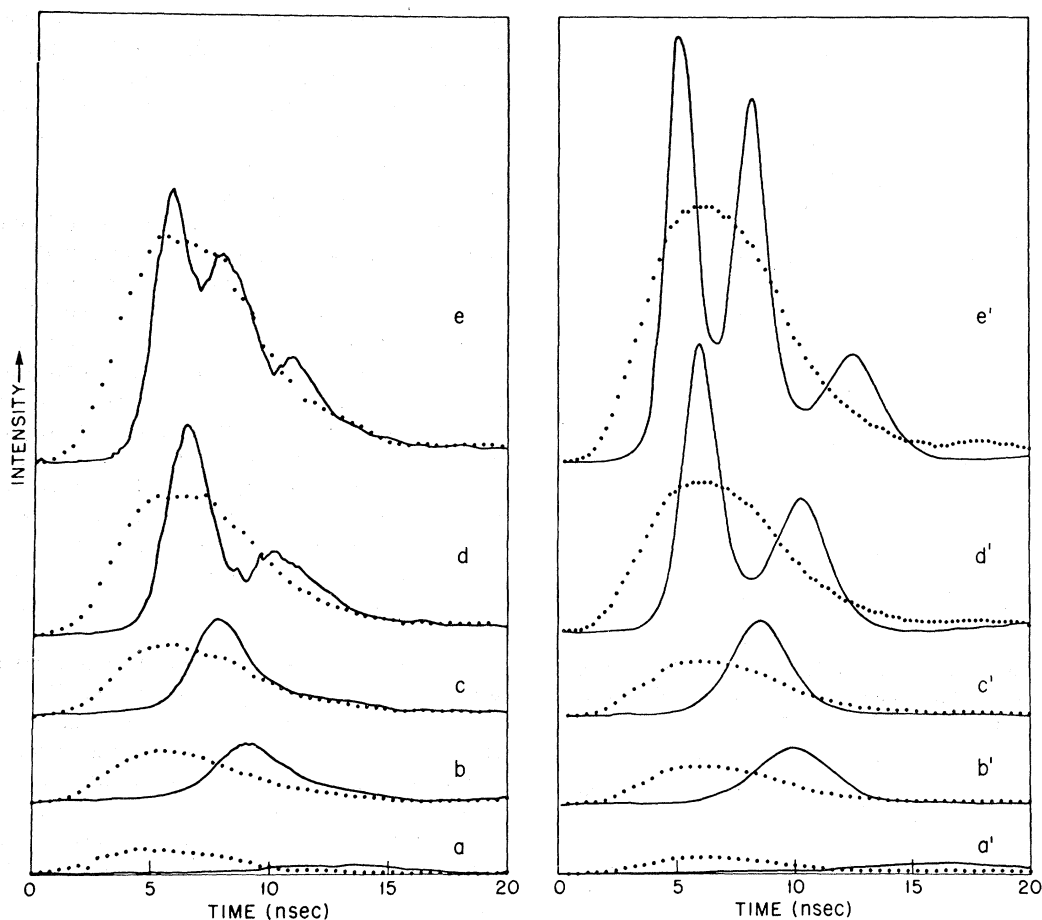


FIG. 3. Input and output pulse shapes for $\alpha L \approx 5$ and uniform-plane-wave conditions. Sampling scope output and input pulses (obtained by rotating quarter wave plate through 90°) are shown in (a)–(e) corresponding to the peace-symbol points in Fig. 13. Computer-generated output pulses are shown in (a')–(e') corresponding to the gun-barrel points of Fig. 13. Many more experimental curves were taken as indicated in Fig. 13 showing the continuous transition from no delay or reshaping to a 6π input pulse. For input intensities a few percent below that of (a) no delay was observed. The maximum delay of about 8–10 nsec occurred just below (a), which has an area above π . Diffraction from the sharp stripped edges of the spatial profile is severe in the extremely nonlinear region around π . This is believed responsible for the lower transmission, higher input intensity, and shorter delay of the point (a) compared with (a') calculated neglecting diffraction. Point (b) is just above 2π with low loss and slight peaking. This almost lossless propagation through an absorber with linear transmission of 0.7% is in excellent agreement with the theory of SIT. Points (c), (d), and (e) show pulse breakup and peaking for inputs of just under 3π and 5π and approximately 6π . The areas given here are the areas for a sech input pulse; the actual areas at the top of Fig. 13 are larger because of the nonhyperbolic secant nature of the input, particularly the long tail. The slightly smaller experimental delays likely result from an actual experimental αL of slightly under the measured value of 5. The change in αL required for complete agreement is well within the experimental uncertainty.

puter results for various input areas are shown in Figs. 3(a')–3(e'). Traces 3(a') through 3(e') correspond to input areas of 5.7, 8.7, 10.5, 17.5, and 23, respectively. In 3(a') the pulse is slightly below 2π and is delayed more than expected by Eq. (12). With the input area 8.7 in 3(b') the output pulse is nearly 2π after reshaping and incoherent decay losses. The reshaping losses are caused by variation from sech and by long experimental pulse tails. In 3(c') the area is nearly 3π at the input and as the pulse evolves toward the stable 2π pulse in

the absorber, it narrows and its peak intensity increases to greater than that of the input pulse (quite remarkable behavior for an $\alpha L = 5$ absorber). In 3(d') the input area is $> 4\pi$ and the pulse evolves to two 2π pulses caused by two complete rotations of the Rb atoms from ground to excited state and back. Finally, in 3(e') the input area is $> 6\pi$ and the pulse is evolving toward three 2π pulses. A number of other input areas were used to compute pulse shapes and energy ratios. The energy ratios are shown in Figs. 2(c) and 13.

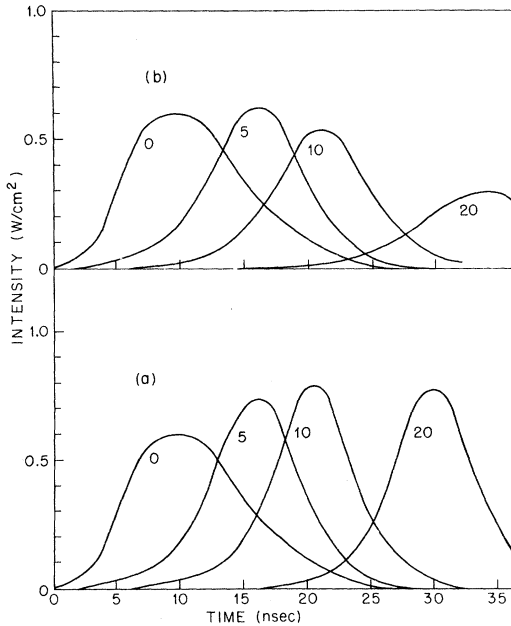


FIG. 4. Evolution of a 2π pulse with experimental input pulse shape using computer solutions with (b) and without (a) incoherent decay, T_1 and T_2' . Parameters are

(a) $T_1 = 2000$ nsec, $T_2' = 5000$ nsec

Area	αL	E_0/E_I
6.28	0	1
6.27	2.5	0.97
6.275	5	0.968
6.278	10	0.966

(b) $T_1 = 33.6$ nsec, $T_2' = 55$ nsec

Area	αL	E_0/E_I
6.28	0	1
6.1	2.5	0.876
6.0	5	0.775
5.8	10	0.568

$2\alpha L$ is labeled on each pulse.

These computer-generated pulses have included all the losses expected experimentally except diffraction. In particular it is interesting to study the effects of T_1 and T_2' on the pulse propagation. This was done on the computer and the results are shown in Fig. 4. In Fig. 4(a), the evolution of a 2π input area pulse is shown with T_1 and T_2' very long (≈ 5000 nsec) compared to the experimental input pulse. Notice the reshaping of the pulse shape to hyperbolic secant with very little energy loss. In agreement with the area theorem [Eq. (13)] the area remains stable at 2π . Using the T_1 and T_2' appropriate for the Rb transition studied here, the 2π input pulse evolves as shown in Fig. 4(b). There is a gradual loss of both energy and area as the pulse lengthens to try to maintain the area at 2π . Eventually the area drops below π and the pulse

loses area and energy rapidly until it reaches the Beer's-law region and is absorbed completely. Note that the delay increases with losses for a 2π incident pulse since the gradual loss broadens the pulse (as it tries to maintain its 2π area) and the area gradually decreases toward π ; both effects tending to decrease the propagation velocity and increase the delay. These results seem to be in conflict with computer solutions by Hopf and Scully,¹⁰ which show a decrease in delay with increased losses. The only relaxation terms included in Ref. 10 are decays to levels *outside* the resonant two-level system. If the relaxation processes are predominantly out of the two-level system to a third level, α may decrease enough during the pulse to cause a decrease in SIT delay for an increase in loss. This may explain the conflict between the calculations shown in Fig. 4 and those in Ref. 10. It is important to remember that pulse delay is also a characteristic shown by incoherent saturation effects, thus it is not a convincing demonstration of SIT.

Further computer studies of focused waves are discussed in Sec. IV C. Computer studies are now in progress to relate to a homogeneously broadened line using pulse lengths much shorter than the inverse homogeneous linewidth. Similar computer studies have recently been made by Estes, Eteson, and Narducci.¹¹ These conditions are of interest for propagation of picosecond pulses in atomic absorbers.

C. Requirements for Optical Pulse and Absorber for Ideal SIT

Before continuing with the experimental details, it is of interest to summarize the limitations imposed on the experiment by the theoretical assumptions. These limitations are summarized in Table I. Computer and analytical SIT solutions assume unique values of ω , $\mathcal{E}(t)$, and p , and thus requirements A1, A2, and B2. Requirements A4 and B4 are coupled since sufficient power can often be attained by decreasing the beam diameter d ; however, when $\alpha d^2/\lambda < 1$ the experiment has the added complications of diffraction. Diffraction in SIT has been included only qualitatively in the theory to date. As will be discussed in Sec. IV B, the SIT effects are largely unaltered if the laser is not at the exact center of the resonance line. However, if the dispersive component of the susceptibility is of the order of the absorptive component, effects like self-focusing¹² may dominate in the experiments.

The Rb-Hg system satisfies all the requirements of Table I, and for the first time SIT experiments can be compared directly with the theory. Recent dye laser developments suggest that frequency and phase-stability requirements can be met and their use should greatly expand the applications of SIT. It is hoped that the Hg-Rb system, which has been

TABLE I. Ideal SIT experimental parameters.

Ideal	Hg-Rb	Other systems
A. Optical pulse		
1. Frequency and phase stability ($\Delta\nu \ll 1/\tau$)	Single-mode gas laser	Dye lasers are recently also able to obtain $\Delta\nu \ll 1/\tau$
2. Plane wave of uniform intensity profile	Aperture and TEM ₀₀ mode	Often lacking in previous experiments
3. Stable coincidence with good absorber	Single isotope in magnetic field	Dye laser is tunable
4. Sufficient power for 2π pulses	$\approx 1-10$ W/cm ² for alkali atoms	
B. Absorber		
1. Homogeneous; variable αL	Gas	Solids (e.g., ruby) may be optically inhomogeneous
2. Unique dipole moment, i.e., no degeneracy	Degeneracy lifted by magnetic field	Confusing in SF ₆
3. $T^* \ll \tau_p \ll T_2^*, T_1$	($0.8 < 5-10 < 56$, 34 nsec)	
4. No diffraction effects $\alpha d^2/\lambda > 1$	$\alpha d^2/\lambda \approx 4$	Often lacking

used to test SIT, will serve as a model for future experiments.

III. EXPERIMENTAL APPARATUS

The actual system chosen to approximate the rather stringent assumptions of the theory (Table I) consisted of a coherent optical pulse from a ²⁰²Hg laser and a single absorption cell of ⁸⁷Rb vapor. The basic components of the system are shown in Fig. 5. The laser is diagrammed as an optical resonator defined by mirrors M_1 and M_2 , a hollow-cathode discharge tube pulsed at 160 pulses per sec, an aperture A_1 for limiting the oscillations to a single transverse mode, and a single-longitudinal-mode selector SMS. A 5–10 nsec portion of the 1- μ sec laser output was gated through the linear polarizer LP by applying a high-voltage pulse V_{PC} to the Pockels cell (PC). The ⁸⁷Rb absorbing atoms composed a vapor of density 10^{11} – 10^{13} atoms/cm³ in the 1–10 mm long cell (C). The 7944.66- \AA output of the Hg laser is separated by 3 \AA from the zero magnetic field absorption of Rb at 7947.64 \AA . At 74.5-kOe magnetic field B , produced by the superconducting solenoid S , Zeeman tuned the Rb absorption to coincide with the laser frequency. This large field also removed the low-field complications arising from the hyperfine interaction between the electron and the nucleus with nuclear spin $\frac{3}{2}$. These hyperfine degeneracies are common to all alkali atoms in zero field. The quarter-wave plate QW transformed the linearly polarized

pulse into absorbable right or unabsorbable left circularly polarized light. The input and output pulses were easily compared by rotating the quar-

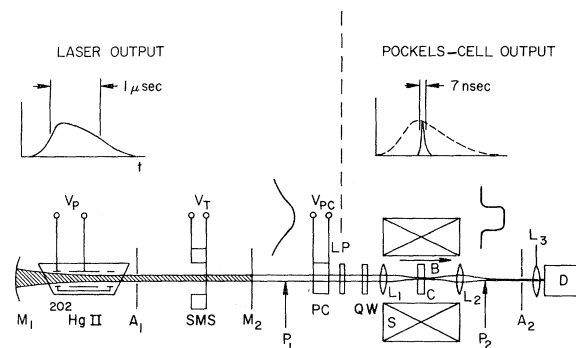


FIG. 5. Schematic diagram of Hg-Rb SIT apparatus. M_1 is a 3-m totally reflecting mirror; V_p is a 1- μ sec voltage pulse causing 1- μ sec single-mode laser pulse; A_1 is the aperture to select TEM₀₀ mode; SMS is single-longitudinal-mode selector; V_T is the mode-tuning voltage across the piezoelectric transducer; M_2 is a 4% transmission flat output mirror; P_1 is the Gaussian transverse intensity profile; PC is the Pockels-cell gating 5–10 nsec portion of the laser pulse; LP and CP are linear and circular polarizers; S is a superconducting selenoid; L_1 , L_2 , and L_3 are imaging lenses; B is the magnetic field (≈ 74.5 kG); C is the Rb vapor cell; P_2 is the stripped Gaussian profile after SIT interactions in the Rb cell; A_2 is the limiting aperture used to observe a uniform transverse intensity; and D is an avalanche photodiode or cross-field photomultiplier detector.

ter-wave plate through 90° . In some cases the input intensity was increased with a lens L_1 , positioned so that the cell was centered in the plane-wave portion of the focal region. Lens L_2 imaged the output of the cell in front of the detector D. An aperture A_2 was usually used to select only the center portion of the output beam originating from the part of the Gaussian input beam approximately satisfying the uniform-plane-wave condition. Lens L_3 focused the output on the fast detector (avalanche photodiode or crossed-field photomultiplier). The temporal evolution of the output pulse was observed with a sampling (or fast Tektronix 519 or 454) oscilloscope. The frequency of the laser was monitored with a Fabry-Perot interferometer and controlled within the laser gain curve by varying the voltage V_T on a piezoelectric stack to which the single-mode selector was attached.

Details of the individual components and discussions of how this system satisfies the restrictions of the ideal assumptions of Sec. IIC comprise the remainder of this section. For a quick reading, look at Secs. IIIA6 and IIIB3 only.

A. Coherent Optical Pulse

1. Laser Construction and Operation

Laser emission at 7945 \AA between the $7p^2P_{1/2}^0$ and $7s^2S_{1/2}$ excited states of Hg II was reported in passing in a detailed article on the characteristics of the doublet companion line at 6150 \AA .¹³ Under contract with Bell Labs, Spectra Physics investigated the characteristics of the 7945-\AA transition.¹⁴ Basically, the laser consists of a 53-cm-long hollow cathode 24 mm in diameter with an anode at each end and containing helium at a pressure of 30 Torr and ^{202}Hg vapor. Excitation with 50-A 6-kV microsecond-long pulses produces comparable length 7945-\AA optical pulses with 6-W peak multimode power through a 4.6% transmission output mirror. Insertion of an aperture of the appropriate diameter limits the oscillation to the TEM_{00} transverse mode which has the lowest diffraction loss. The transverse mode patterns were observed with a Seed Electronics model B infrared image converter.

The Spectra Physics design was modified to increase the frequency stability and output power. The cavity was lengthened to 287 cm using four Invar rods, a 3-m-rad maximum-reflectivity mirror, and the 4.7% transmitting flat mirror. This approximately doubled the single-transverse-mode power by better filling of the large-diameter gain medium situated near the spherical mirror. The entire laser was mounted on a 3-in.-thick slab of aluminum supported by four Firestone 110B Air-mount tires attached to a sturdy wooden table. Without this vibration damping the longitudinal

mode frequencies fluctuated wildly.

2. Single Longitudinal Mode

The use of the single isotope ^{202}Hg in the laser resulted in a Doppler width of 350 MHz and a gain curve only slightly wider. The large atomic mass, long wavelength, and low temperature ($\approx 80\text{--}100^\circ\text{C}$ for the hollow Kovar cathode) are responsible for this small Doppler width. Nonetheless, a frequency stability of at least ± 50 MHz is needed to maintain the laser frequency approximately centered within the Rb 552-MHz Doppler width. Since the longitudinal cavity modes are separated by $c/2L \approx 52$ MHz, it is clear that restriction to a single longitudinal mode is needed. The presence of more than one longitudinal mode would greatly complicate the interpretation of the SIT experiment.

A very simple but effective single-mode selector (SMS) was suggested by Troitskii and Goldina¹⁵ and further investigated by Smith, Schneider, and Danielmeyer.¹⁶ A metallic film, thin compared with the optical wavelength, is inserted in the cavity near the flat mirror, forcing a node in the electromagnetic field. The film-flat distance is chosen so that the mode spacing of this short cavity is just greater than the frequency width of the gain medium in order to optimize its mode selectivity. Then the film-flat distance is varied to select the desired longitudinal mode of the long cavity lying within the gain curve. In this experiment a 50- \AA Nichrome film was evaporated on a high-quality quartz flat, affixed to a Lansing piezoelectric stack, and inserted 30 cm from the flat mirror.¹⁷ The effectiveness of this SMS is demonstrated in Fig. 6 in which the spectral output of the laser is displayed for various mode conditions.

3. Frequency Detection

The frequency profiles were observed with a piezoelectric scanned Fabry-Perot interferometer containing two flats with reflectance $R = 0.985$ separated by about 5 cm. The output of the Fabry-Perot was focused by a lens of focal length $f = 30$ cm onto a pinhole of diameter $d = 50 \mu\text{m}$; the resolution of the pinhole was then about $\Delta\nu_p = cd^2/8\lambda f^2 \approx 1.3$ MHz. The reflecting finesse is expected to be $N_R = \pi\sqrt{R}/(1-R) \approx 208$.¹⁸ The nonflatness finesse for the $\lambda/200$ flats should certainly be greater than the calculated $N_0 = 100$ over the small diameter of the laser beam.¹⁸ These theoretical contributions to the finesse are then consistent with an experimental lower limit of 100 determined with a short spacing. The frequency resolution with a spacing $t = 5$ cm was then the free spectral range $F = c/2t = 3000$ MHz divided by the finesse or about 30 MHz. The transmission through the pinhole was detected by an Amperex 56TVP or RCA 31000F photomultiplier.

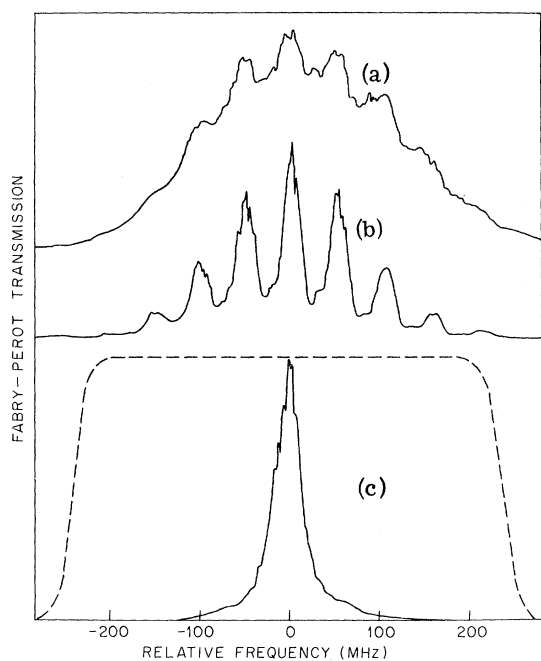


FIG. 6. Fabry-Perot interferometer transmission of the laser output under the following operating conditions: (a) multimode, (b) single transverse mode, and (c) single transverse and longitudinal mode. The vertical scale is not the same in the three curves. The respective integrated powers were 280, 60, and $20 \mu\text{W}$. The width in (c) is the Fabry-Perot instrumental width. The dashed curve in part (c) gives the laser output as its frequency is scanned by moving the single-mode selector (and the spherical mirror unless discrete frequency steps are desired). Notice that peak output occurs over a much wider frequency range when the SMS is present. The traces were taken with a PAR 160 Boxcar with a scanning rate of about 8 MHz/sec.

The Fabry-Perot plates were carefully aligned perpendicular to the laser beam to increase the coupling into the Fabry-Perot modes. A neutral density attenuator between the interferometer and laser prevented feedback into the laser. The laser frequency was usually monitored without reducing the maximum power by using the $1\text{-}\mu\text{sec}$ pulse deflected at right angles by the Glans prism labeled LP in Fig. 5.

Temperature changes can alter the transmission frequency of the Fabry-Perot by varying the effective spacing. Invar expansion shifts the transmission by $-0.3 \text{ GHz}/^\circ\text{C}$. Changes in the index of air from density changes at constant pressure amount to almost $0.4 \text{ GHz}/^\circ\text{C}$. The Fabry-Perot etalon was placed inside a vacuum chamber to prevent air current instabilities and greatly reduce and slow down temperature variations of the invar rods. Evacuation did improve the Fabry-Perot stability substantially. But an annoying and still unexplained lengthening of the spacing makes the

fixed-frequency laser gain profile appear to shift to higher frequencies at about 50 MHz/h.

4. Frequency Selection and Stabilization

The laser frequency was then tunable in discrete steps of 52 MHz by scanning the SMS through the longitudinal modes within the gain curve. The frequency could be varied by 400–500 MHz in this manner. This tunability was particularly advantageous during the runs with a superconducting magnet operating in the persistent mode; the slow decrease in field could be compensated by a decrease in laser frequency. It was also useful for locating the center of the ^{87}Rb absorption line as shown in Fig. 7. If the absorption center frequency lay within the gain curve and the peak absorption was in a reasonable range (10–99%), the center frequency could be located within 50 MHz. By periodic relocation of the center frequency and periodic monitoring of the lasing mode and its position within the gain curve, the laser and absorber frequencies were held equal within $\pm 50 \text{ MHz}$ throughout the data taking. This corresponds to a long-term frequency stability of $\pm 0.13 \text{ ppm}$; only recently has a dye laser stability approaching this value ($\pm 0.42 \text{ ppm}$) been reported.¹⁹ Clearly stable tunable sources will permit the extension of coherent optic experiments to a great variety of absorbers. Meanwhile, much has been and can be demonstrated and learned with the ^{202}Hg single-frequency gas laser.

The amplitude of the laser pulse was monitored with an RCA 7102 photomultiplier. Whenever the SMS mode was not centered on a longitudinal mode, more than one of the longitudinal modes lased resulting in a decrease in the amplitude of the laser pulse. The signal-to-noise ratio of the sampling oscilloscope pulse traces was increased by accepting for sampling only those pulses arising from a laser pulse with amplitude within a few percent of the maximum amplitude. This discrimination was accomplished with a Tektronix 454 oscilloscope.

After the experiment of Ref. 1, the entire laser was placed in a vacuum chamber, lengthening the time between longitudinal mode jumps. The index

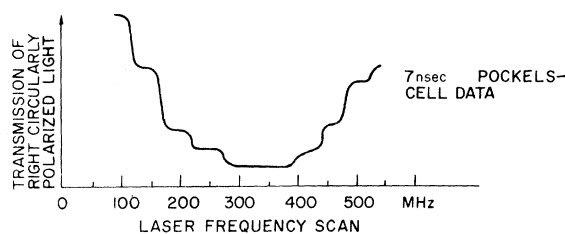


FIG. 7. Absorption of the laser light by Rb^{87} at low light intensities as the laser frequency is tuned through the longitudinal modes by the SMS. Each discrete step corresponds to a new longitudinal mode.

gradients in the vicinity of the hot Brewster windows were eliminated. Evacuation also buffered the laser against room drafts and temperature changes.

5. Short Pulse Production and Attenuation

The discharge-tube Brewster windows resulted in a linearly polarized laser output. A Korad Pockels cell and Glans-prism linear polarizer were then sufficient to gate on a 5–10-nsec portion of the 1- μ sec laser pulse. The laser trigger pulse also triggered a Hewlett-Packard pulse generator (222A or 1900 system) which triggered a Kappa Scientific Corp. model KT-1000 sync pulse generator after a variable delay. The KT-1000 drove a Kappa model PG-5 high voltage pulse generator powered by a Kappa Thyatron control unit and a Sorensen high-voltage power supply. The PG-5 output was shaped with a 5- or 10-nsec Kappa NPF plug-in pulse network. A 10-nsec plug-in was used with double passage of the optical pulse through the Pockels cell to obtain the 7-nsec pulse of Ref. 1. In the compression experiment single passage with the 10-nsec plug-in was the normal mode of operation although the 5-nsec plug-in was used briefly. Secondary peaks on the output of the 5-nsec plug-in reduced its usefulness.

The variable delay between the laser trigger and the Pockels-cell actuation was utilized as a variable attenuator since the long laser pulse decreased to zero in a microsecond but maintained the same mode structure. This method of attenuation was rapid and did not deflect the beam as do neutral density filters.

In the early work, a Kerr cell was employed rather than a Pockels cell. What appeared to be pulse breakup occurred over too great a range of input intensities to be the simple breakup predicted by McCall and Hahn² and later seen with a Pockels cell.¹ The phase shifts introduced by the Kerr cell might be responsible. It is shown in Appendix C that a Pockels-cell shutter does not introduce a time-dependent phase shift as does a Kerr cell. The lack of a significant phase shift or chirp on the optical pulse of this experiment was demonstrated by

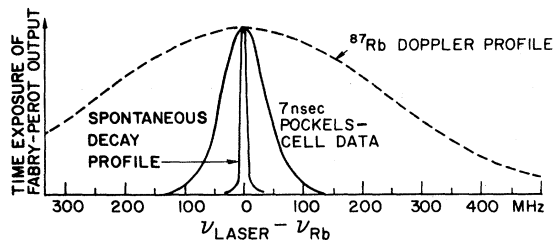


FIG. 8. Comparison of the ^{87}Rb Doppler absorption profile, the spectral profile of the Pockels-cell pulse, and the natural width of the ^{87}Rb absorption from radiation damping.

mixing the pulse with the much longer laser output pulse (see Appendix C).

A final check on the spectral purity of the input pulse was a Fabry-Perot scan yielding a frequency spread of about 80 MHz. That scan is compared with the ^{87}Rb absorption in Fig. 8. The width agrees well with the Fourier transform of the 6.5-nsec input pulse envelope convolved with the Fabry-Perot instrument function with a width of 25–30 MHz. Again any chirp during the pulse could be no more than a small fraction of a radian.

6. Comparison with Ideal Optical Pulse

Referring back to Table I, one can compare the actual Pockels-cell pulse with the characteristics of the ideal optical pulse. First, the frequency and phase stabilities are excellent; the spectral profile of the pulse is the Fourier transform of the pulse envelope. Second, the laser output is a plane wave of Gaussian spatial profile. The uniform profile condition is approximated by an aperture. The Gaussian profile permits a demonstration of the importance of the uniform condition. Third, there is a stable coincidence with ^{87}Rb in a 74.5-kOe magnetic field which approximates closely an ideal absorber (Sec. III B). Fourth, sufficient power for pulses with areas of several π is achieved by weak focusing of the laser beam. For the transition used in Rb, a 2π square pulse of width $\tau_p = 7$ nsec corresponds to an intensity of 2.8 W/cm^2 (see Sec. III B2). A peak intensity of about 25 W/cm^2 was obtained by focusing the 1-mm-diam beam to 116- μm full width at half-maximum (FWHM). By placing a short (1-mm) Rb cell in the center of the focal region, the plane-wave condition was approximated closely. Table I summarizes the manner in which the present optical pulse closely approximates the ideal pulse.

B. Simple Atomic Absorber

1. Rb in a Strong External Magnetic Field

In low magnetic fields the eight ^{87}Rb magnetic substates of the $^2S_{1/2}$ ground state have many unresolved transitions to the $^2P_{1/2}$ excited state (see Fig. 9). Each transition of different dipole moment would be driven at a different rate by a coherent optical field and SIT would be quite complicated.^{5,20} It is then fortunate that a strong magnetic field is required to bring the Rb absorption into coincidence with the $7944.66\text{-}\text{\AA}$ ^{202}Hg II laser because the level degeneracy is lifted.

In a strong external field the energy levels are given approximately by²¹

$$W(M_I, M_J) = -\mu_J H_0 M_J / J - \mu_I H_0 M_I / I + h a M_I M_J, \quad (30)$$

where the electrons and nuclei have total angular momenta \vec{J} and \vec{I} with projections M_J and M_I along

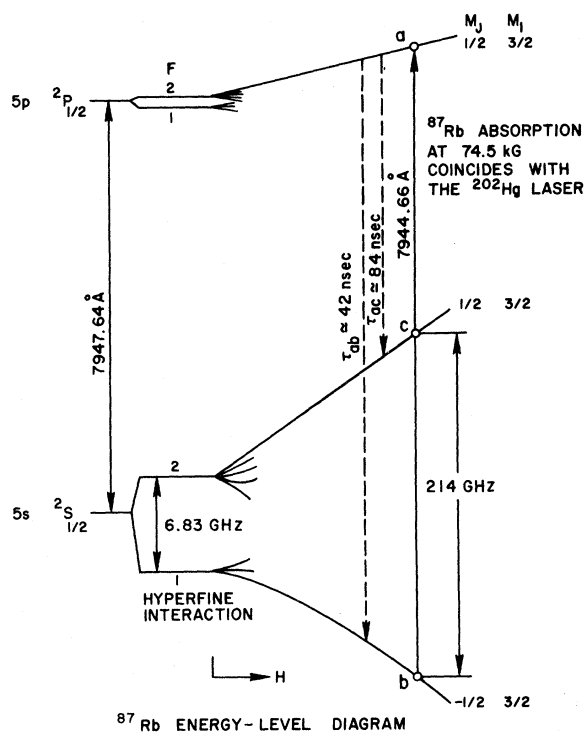


FIG. 9. Diagram of the relevant energy levels of ^{87}Rb as a function of magnetic field strength. The Zeeman interaction at 74.5 kOe lifts the low-field degeneracy and increases the absorption frequency to coincide with the laser emission frequency.

the external field H_0 and have magnetic moments μ_J and μ_I . The hyperfine separation $\Delta\nu_{\text{HF}}$ is equal to $(I + \frac{1}{2})a$. The values of $\Delta\nu_{\text{HF}}$ are 6.83, 0.816, 3.04, and 0.36 GHz for the $5s\ ^2S_{1/2}$ and $5p\ ^2P_{1/2}$ states of ^{87}Rb and of ^{85}Rb , respectively.²² The hyperfine and external field contributions to the

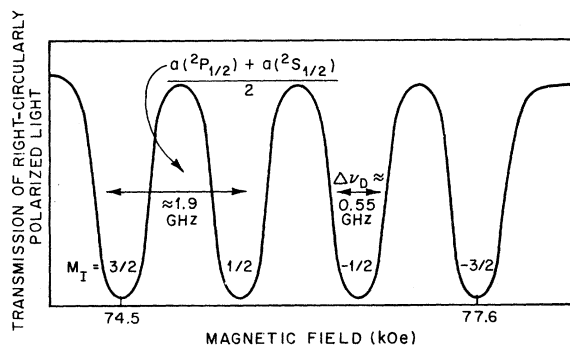


FIG. 10. Absorption of the ^{202}Hg laser output as a function of magnetic field strength at the ^{87}Rb absorbers. The absorption width is greater than the Doppler width because the light intensity was too large to avoid nonlinear transmission. The frequency width of the short laser pulse also contributed to the observed absorption width.

frequency separation between a substate ($M_J = -\frac{1}{2}, M_I$) of the ground state and substate ($M_J = +\frac{1}{2}, M_I$) of the excited $^2P_{1/2}$ state are then

$$\begin{aligned} & \frac{\mu_0 H_0}{2h} [g_J(^2S_{1/2}) - g_J(^2P_{1/2})] \\ & + \frac{M_I}{2I+1} [\Delta\nu_{\text{HF}}(^2P_{1/2}) + \Delta\nu_{\text{HF}}(^2S_{1/2})] \\ & \approx (1.867 \text{ MHz/Oe}) H_0 + (1.915 \text{ GHz}) M_I \\ & \quad \text{for } ^{87}\text{Rb} (I = \frac{3}{2}) \\ & \approx (1.867 \text{ MHz/Oe}) H_0 + (0.567 \text{ GHz}) M_I \\ & \quad \text{for } ^{85}\text{Rb} (I = \frac{5}{2}). \quad (31) \end{aligned}$$

The electronic Zeeman effect is responsible for most of the 3-Å level shift needed for coincidence. But it is the second term of Eq. (33) which is crucial for resolving the transitions of different M_I . For ^{87}Rb the four components are well resolved with a separation of about 3.5 Doppler widths (see Fig. 10). The six components of ^{85}Rb on the other hand have a separation of only one Doppler width. The ^{85}Rb absorption is then inhomogeneous and almost uniform over about 3 GHz (see Fig. 11).

Two different superconducting magnets have been used. The first did not have straight-through access, so it was necessary to enter and leave the magnet through the same opening about a meter from the center of the magnet. The alignment of the beam through the necessary optics and of the two mirrors at the bottom of the magnet insert was difficult and time consuming. With the magnet operated in its persistent mode the rate of field decrease was about 20 MHz/h. The laser frequency was kept in coincidence by adjusting its frequency

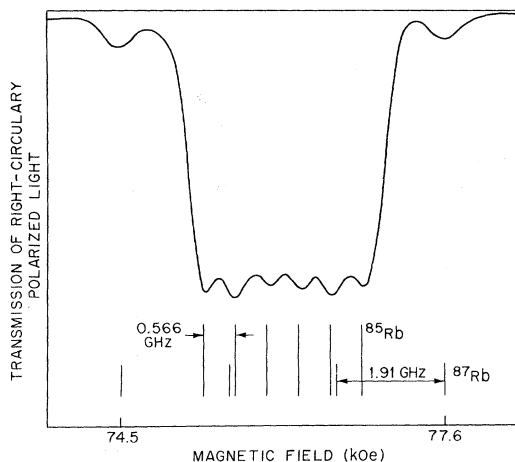


FIG. 11. Absorption by ^{85}Rb with a small impurity of ^{87}Rb . The theoretical spacings and relative strengths of the absorption lines for natural Rb are also shown. Isotope shift is neglected.

with the SMS. About once a day, the magnetic field was increased to reset the Rb absorption to the high-frequency side of the laser gain curve. The operation of the second superconducting magnet was simplified by its straight-through access and its low-helium-loss normal-mode operation. This permitted rapid field scanning and recentering of the absorption on the laser emission. The magnet access tubes, in which the Rb absorption cell and heaters were placed, were evacuated to eliminate deflections of the laser beam by index fluctuations resulting from air flow around the 100 °C heaters.

2. Electric Dipole Moment

It is shown in Appendix D that from the 28-nsec measured lifetime of the Rb $^2P_{1/2}$ excited state one finds a 42-nsec partial lifetime from the $5p^2P_{1/2}$ ($M_J = +\frac{1}{2}, M_I$) substate $|a\rangle$ to the $5s^2S_{1/2}$ ($M_J = -\frac{1}{2}, M_I$) substate $|b\rangle$ and 84 nsec to the $5s^2S_{1/2}$ ($M_J = +\frac{1}{2}, M_I$) substate $|c\rangle$. The electric dipole moment of the transition $a \rightarrow b$ is then shown to be 4.35×10^{-18} esu cm.

The intensity I required for a 2π square pulse follows immediately:

$$(2p/\hbar) \int \mathcal{E} dt = (2p/\hbar) \mathcal{E}_M \tau_p = 2\pi, \quad (32a)$$

$$I = c |\mathcal{E}_M|^2 / 4\pi = c \pi \hbar^2 / 4p^2 \tau_p^2 = 2.8 \text{ W/cm}^2, \quad (32b)$$

with $\tau_p = 7$ nsec.

3. Comparison with Ideal Absorber

The characteristics of the ideal absorber (summarized in Table I) are approximated by ^{87}Rb in a strong magnetic field as follows: First, the Rb vapor is homogeneous (statistical fluctuations are $< 0.5\%$), and its density can easily be varied with temperature. Second, a strong magnetic field lifts the low-field degeneracy, yielding a simple two-level absorption transition with a unique dipole moment of 4.35 D. Third, the pulse length τ_p of 7 nsec is long compared with the inverse inhomogeneous width of 0.8 nsec; this ensures a uniform absorption over the Fourier frequency spread of the pulse as shown in Fig. 8. The coherence damping time, related to the excited spontaneous decay time of 28 nsec, is long compared with τ_p , as it must be if coherence effects are to be studied. Fourth, an absorption coefficient of 100 cm^{-1} or more can be achieved in a cell only 1 mm long. This is much shorter than the plane-wave portion of the focal region of the 38-cm lens used to obtain sufficient input power. This was verified by measuring the beam diameter as a function of distance from the cell. In summary, the absorber chosen is an excellent approximation to the ideal absorber as summarized in Table I. Two slight departures are included in the computer simulations (see Sec. II): first, weak coupling to a third

level by spontaneous emission (84 nsec) and second, relaxation losses between the levels by spontaneous emission (42 nsec).

C. Detection Equipment

The optical-pulse detector most often used was a Texas Instruments TIXL59 silicon avalanche photodiode with a gain of 100 and quantum efficiency approaching 100% at 7945 Å. Its distortion of a 1-nsec mode-locked He-Ne laser pulse consisted of a 0.3-nsec increase in width and a 10% undershoot after the pulse. In the compression experiment a Sylvania Model 502 GaAs crossed-field photomultiplier was used. It was slightly faster than the TIXL59 and had a gain of 7×10^3 and a quantum efficiency of a few percent at 7945 Å. Its response width was checked to be less than 0.4 nsec with an Ar mode-locked laser. The time response of the photodiode is a sensitive function of the focusing of the light onto the detector required by the small active area (≈ 0.6 mm for the TIXL59). Light falling on the sides of the detector exhibits a much longer time constant. Thus, if focusing and aperturing is not done carefully short pulses may appear to have extended "tails."

The detector outputs were monitored with a Hewlett-Packard 141A sampling oscilloscope with 0.3-nsec rise time or a Tektronix 564 oscilloscope with 3T2, 3S2, and S-2 plug-ins with a 75-psec rise time.

A Cintra Model 101 quantum radiometer with model 1394 filter spectroradiometer probe made the low-level power measurements simple.

IV. EXPERIMENTAL RESULTS AND DISCUSSION

A. Plane Wave

In Sec. III it was shown that the Hg-Rb system is a close approximation to the ideal system for demonstrating SIT as discussed in Sec. II. The uniform-plane-wave theory of SIT predicts a number of interesting features of the coherent interaction of an optical pulse with an absorber. The features demonstrated here are nonlinear transmission, large delays, pulse breakup, and peak amplification.

1. Nonlinear Transmission

A greater than linear increase in output energy for an increase in input energy characterizes other nonlinear phenomena such as saturation in addition to SIT. The mere observation of nonlinearity is then poor evidence for SIT. But a careful comparison of the experimental data with theory in the nonlinear region is useful as a check on the theoretical threshold power and the shape of the nonlinearity.

The nonlinear transmission under approximately uniform-plane-wave conditions is shown in Fig. 12

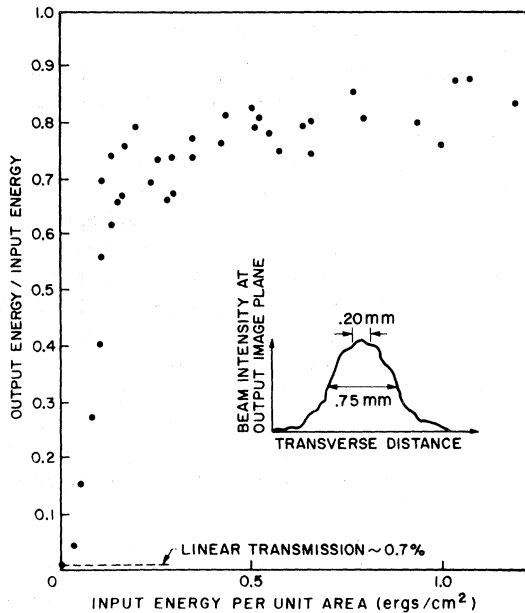


FIG. 12. Demonstration of nonlinear transmission on the onset of SIT in ^{87}Rb vapor. An aperture selected the approximately uniform portion of the plane-wave beam.

for an αL of 5, $L = 1$ mm, and an input pulse about 7 nsec wide (shown in Fig. 15). A 38-cm lens focused the beam to a plane wavefront with Gaussian intensity profile of 110- μm full width. A uniform spatial intensity profile was approximated by selecting only the center portion of the output as shown by the inset. The relative input and output energies were measured by electronically integrating²³ the area of the pulse shape as the sampling oscilloscope storage was scanned at a uniform rate. The 0.7% linear transmission was measured with a PAR 160 Boxcar using 1- μsec laser pulses attenuated well below the SIT threshold.

The experimental nonlinear transmission data are compared with a computer simulation (as discussed in Sec. II) in Fig. 13. The absolute power calibration is in good agreement with theory as discussed in Sec. IV A6. The 2π pulse transparency is not 100% because the input pulse shape is not sech and must be reshaped, and because spontaneous emission losses gradually destroy any coherence. Diffraction losses and imperfect satisfaction of the uniform-plane-wave assumption are believed responsible for the slightly lower transmission in the experimental case. Violation of the uniform-plane-wave condition is dramatized by the much slower increase in nonlinear transmission when a Gaussian spatial input profile is used. Most previous experiments have been for a Gaussian profile, making comparisons with plane-wave theories rather meaningless. The data of Fig. 12 suggest a decrease

in the transmission between 2π and 4π in agreement with theory (see Secs. IV A3 and IV A4, where the pulse shapes are discussed). The horizontal uncertainties in Fig. 12 are certainly less than half of the vertical uncertainties which arise from the ratio of numbers; the output energy has larger fluctuations because of the nonlinearity. This 3π decrease in transmission was reproducible. The theoretical predictions and experimental data for the nonlinear transmission are then in good agreement.

2. Large Delays

A second prediction of SIT theory is a propagation velocity for the peak intensity of a 2π pulse much slower than the velocity of light in the absence of SIT. Figure 14 is a pictorial diagram of this delay mechanism. The energy which is absorbed from the pulse in coherently exciting all of the atoms is coherently returned to the trailing edge of the pulse with no loss but with a delay τ_D of about half a pulse-width τ for each absorption length $1/\alpha$ in the sample of length L , i.e., $\tau_D \approx \frac{1}{2} \tau \alpha L$. Or more rigorously, $\mathcal{E} \propto \text{sech}[(t - z/V)/\tau]$, $d\mathcal{E}^2/dz \rightarrow 2\mathcal{E}^2/\tau V$ for $t \rightarrow -\infty$. But the leading edge of the pulse is in the linear regime so $d\mathcal{E}^2/dz = -\alpha\mathcal{E}^2$, i.e., $1/V = \frac{1}{2} \alpha \tau$ or $\tau_D = L/V = \frac{1}{2} \alpha L \tau$. Actually τ is the full width at half-maximum τ_P divided by 1.76.

In Fig. 15 is shown an experimental output pulse of width $\tau_P = 3.8$ nsec delayed by 3.3 nsec from the input pulse by SIT in Rb with $\alpha L = 5 \pm 1.5$. Taking

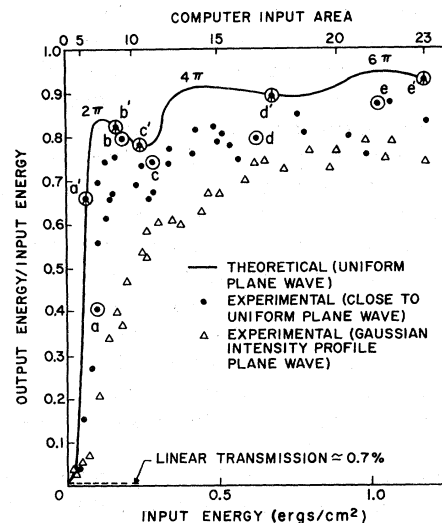


FIG. 13. SIT nonlinear transmission in Rb vapor. Solid curve is a uniform-plane-wave computer solution. Solid dots are data taken with 200- μm output aperture to approximate uniform plane wave. Triangles are data with no aperture corresponding to a plane-wave input with Gaussian intensity profile. The pulse shapes for the circled points are shown in Fig. 3.

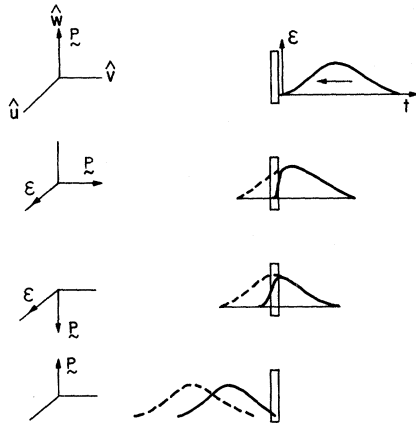


FIG. 14. Pictorial description of one rotation of the macroscopic polarization vector \hat{P} by a coherent electric field with envelope \mathcal{E} , as seen in the rotating frame. The 2π sech input pulse with characteristic width τ is delayed by τ_D but not attenuated by its coherent interaction with an ideal absorber of length L and absorption coefficient α .

$\tau_p = 3.5$ nsec with detector response subtracted, $\tau_D \approx \frac{3}{2}(3.5/1.76) = 5$ nsec. A delay of only 3.3 nsec is observed. Later discussion will show that for Fig. 15, which is also Fig. 3(b), the input area was about 2.5π and that αL was slightly less than 5; both effects would reduce the 5-nsec predicted delay. Delays of ≈ 10 nsec were seen in the maximum delay region around an input area of π . Delays of 20 nsec were seen at higher αL 's. One could make plots of delay vs input area as a comparison between experiment and theory, but it seems more exacting to compare the total pulse shape including breakup and peaking as is done in Secs. IV A3–IV A5.

The 3.3-nsec delay in Fig. 15 is 1000 times longer than the 3.3-psec transit time for the same pulse through an evacuated cell of the same length of 1 mm. The linear dispersive delay is negligible compared with the SIT delay.²⁴ The production of a delay of several nanoseconds by a simple very short absorber may well find application in the miniaturization of optical electronics. For example, the spatial lengths of the input pulse in vacuum and the SIT propagating pulse in the absorber are 200 and 0.1 cm, respectively.

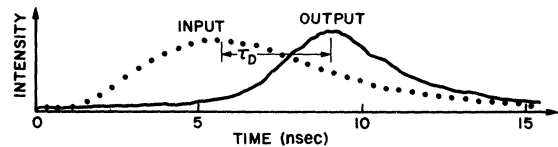
It should be emphasized that large delays also occur for saturation phenomena so that they are not conclusive evidence of SIT either. For example, a saturation effect was observed in Rb when the 1- μ sec pulse irradiated the sample. At an intensity too low to saturate the b to a transition in Fig. 9, the atoms were optically pumped from the state b to the state c via a as in conventional optical pumping. An apparent delay of several tenths of a microsecond resulted (Fig. 16).

3. Pulse Breakup

A third prediction of SIT theory is the decomposition of a pulse with area between $2\pi n - \pi$ and $2\pi n + \pi$ into n propagating 2π pulses. An example of the experimentally observed breakup of a 4π pulse into two 2π pulses is presented in Fig. 17. In a manner analogous to Fig. 14, one could argue that a 4π pulse coherently excites and deexcites the atoms twice. The breakup or dip in intensity occurs because the 2π to 3π part of the pulse is absorbed and reemitted at a later time. The second 2π pulse is less intense and broader because it is returned to the pulse by the driving action of the 3π to 4π part of the pulse which is much less intense and longer than the strong narrow π to 2π portion which stimulates the first 2π pulse. The importance of the uniform-plane-wave condition for the observation of pulse breakup is clearly reemphasized by Fig. 17. Breakup of 6π pulses is shown in Sec. IV A5. Pulse breakup would seem to be a unique signature of SIT. For highly reproducible breakup of a single frequency input pulse as in the present experiment such would seem to be the case. But anything might be seen in the case of single pulse outputs where the input may consist of several frequencies from different longitudinal modes and regions of greatly differing transverse intensities.² The results of this experiment are then the first definitive demonstration of pulse breakup in SIT.²⁵

4. Peak Amplification

SIT theory predicts that for certain values of the input area the peak of the output intensity exceeds the peak of the input intensity. The total output pulse energy is less than the total input pulse energy, of course. This amplification effect is believed to be a unique signature of SIT, an effect difficult to produce or explain without the coherent interaction and mutual coupling between atomic dipoles and coherent light. Certainly no saturation theory



	VACUUM	⁸⁷ Rb WITH $\alpha L = 5$
TIME TO TRAVERSE 1mm CELL	$\frac{L}{c} \approx 3.3$ psec	$\tau_D = 3.3$ nsec
VELOCITY	c	$\frac{L}{\tau_D} \approx c/1000$
SPATIAL LENGTH OF PULSE	$\tau_p c \approx (7\text{nsec})c = 200$ cm	APPARENT INDEX = 1000 $\tau c/1000 \approx 0.1$ cm

FIG. 15. SIT pulse delay in Rb vapor. The input area is close to 2.5π ; $\alpha L \approx 5$. The input pulse is obtained by rotating the quarter wave plate through 90° ; this rotation does not change the pulse in the absence of the Rb.

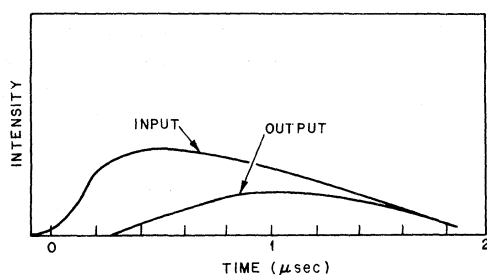


FIG. 16. Optical-bumping saturation effect in laser-irradiated Rb.

can predict peaking of a pulse in traversing a simple two-level absorber. Slight peaking can be seen in Fig. 15 for a 2.5π pulse and substantial peaking for the 4π to 5π pulse of Fig. 17. If a single output pulse is desired, maximum peaking occurs for an area of just under 3π .

The output pulses for 2π and 3π input pulses are compared qualitatively in Fig. 18. The peaking in the 3π case is understood by noting that the energy coherently absorbed in exciting the atoms by the $0-\pi$ portion of the pulse is coherently stimulated to return to the pulse by the short intense $\pi-2\pi$ portion of the input pulse. The 2π pulse so emitted is then shorter and consequently more intense than the 2π pulse emitted by the relatively longer and

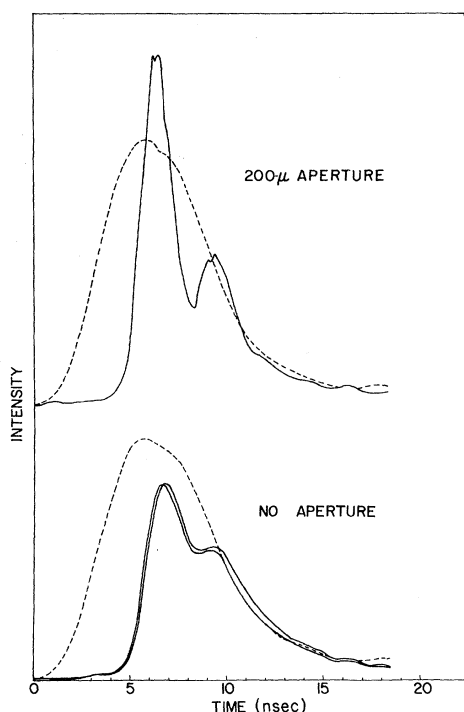


FIG. 17. SIT pulse breakup in Rb vapor with and without uniform transverse intensity profile. These data were taken for an αL of 8-10.

weaker $\pi-2\pi$ portion of the 2π input pulse. On the other hand the $2\pi-3\pi$ portion of the 3π input pulse is lost by this simple argument, in agreement with the dip in transmission in Fig. 13. Figure 3(c) is an experimental illustration of a peak amplification of $\frac{1}{3}$ for an input pulse with area just below 3π . The time compression of over two is even more dramatic at higher αL 's if a spherical wave is used to overcome losses and compel reshaping (see Sec. IV C).

5. Summary of Plane-Wave SIT

Figure 3 summarizes the changes in output shape and intensity as a function of input intensity for a 1-mm-long ^{87}Rb absorption cell with $\alpha L \approx 5$ in the plane-wave focal region of a 38-cm lens. The beam diameter was about $116 \mu\text{m}$ in the cell; the exit of the cell was magnified 6.5 times and apertured by a $200\text{-}\mu\text{m}$ diameter hole to select the uniform portion of the output. Almost identical SIT effects were observed in the second magnet with the same optics and αL but with a 1-cm-long cell.

Somewhat more spectacular breakup and peaking have been observed with a sampling oscilloscope under conditions similar to those of Fig. 3 but with less well-known parameters; for example, see Figs. 19 and 20.

The experimental demonstration of SIT in Rb is

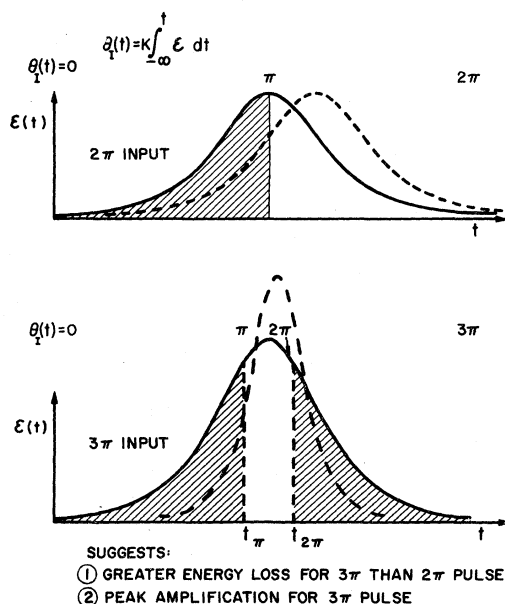


FIG. 18. Simple comparison of 2π and 3π sech input pulses. Peaking occurs for the 3π case because the excited atoms are stimulated to reemit in the short time t_π to $t_{2\pi}$ when the input is maximum. Since the output pulse has area 2π with a width not much longer than $t_{2\pi} - t_\pi$, its peak must be higher than the input peak which occurs in the t_π to $t_{2\pi}$ time interval in which the input area is only π .

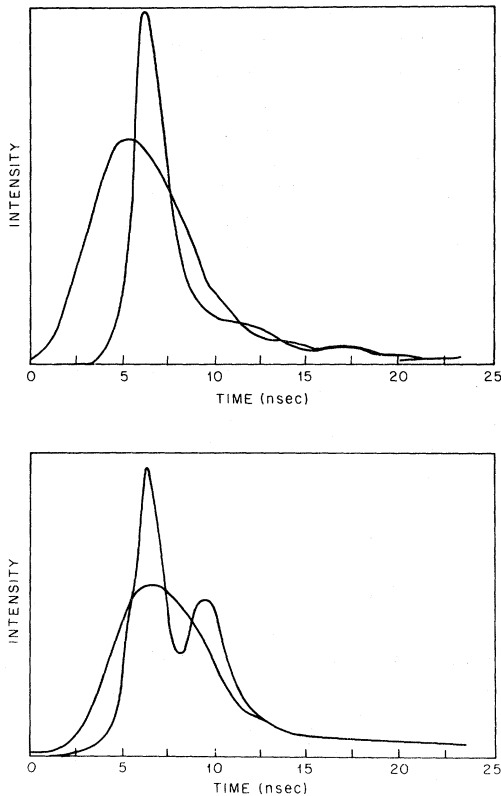


FIG. 19. Other examples of peaking and pulse breakup under conditions similar to Fig. 3 but at higher αL .

then in excellent agreement with the theory as proposed by McCall and Hahn and extended to Rb in Sec. II. The absence of adverse transverse effects is discussed in Sec. IV A7. The stability of the effect for a pulse applied off resonance is shown in Sec. IV B. The absence of chirp in the output is also discussed in Sec. IV B.

6. Absolute Power Calibration

The experimental data of Fig. 13 were plotted with the measured relative input intensities but with an absolute intensity chosen so that the shapes of the experimental and computer outputs looked the same for the same input. In order to make a careful comparison of theory with experiment it is important to compare the absolute input energies. An earlier absolute measurement of the power which was in excellent agreement with the above fitting procedure will now be described. The absolute power calibration was made in several steps since the average power reaching the cell was too low to measure directly. The average power emerging from the laser in 1- μ sec pulses at 160 pulses per sec was about 10 μ W as measured with a Cintra radiometer. Only about 0.8×10^{-3} of that power was transmitted through the Pockels cell shutter; this

ratio was determined from the areas of the 7-nsec and 1- μ sec pulses. Measured losses in the optics further reduced the energy per pulse reaching the Rb vapor to 2.5×10^{-4} ergs. This energy was distributed over a Gaussian transverse spatial profile of width 116 μ m. The energy per unit area in the central, approximately uniform portion, was then about (1.6 ± 0.8) ergs/cm². The corresponding computer-calculated energy per unit area in Fig. 17 is 1.19 ergs/cm². The agreement is well within the uncertainty of the measurement. The measured value is expected to be high because the experimental pulse was not quite zero beyond 20 nsec as assumed for the computer and because the power measurement was for optimum alignment which is then an upper limit. It was shown in Secs. IV A3 and IV A4 that the 1.19-ergs/cm² point with area equal to 23 looks like a 6π pulse. The 7-nsec square-pulse calculation of Sec. III B2 gives 25 W/cm² for a 6π pulse or 1.76 ergs/cm². But the actual pulse has an intensity equivalent width of about 7.5 nsec and an electric field equivalent width of 10.9 nsec, where the equivalent width is for a rectangular pulse of the same maximum value and area. Then calculating the energy flow for a 10.9-nsec rectangular pulse, one has 0.73 ergs/cm². The larger energy needed in the computer solution arises from the fact that for the output to appear as a 6π pulse the input area must be $23 = 7.3\pi$ because the input shape is not sech and because there is an appreciable tail on the pulse which is included in the computer area but contributes little to the formation of a 6π output pulse.

7. Transverse Effects

By scanning the detector aperture across the beam one effectively changes the input intensity; the output pulse shape changes with intensity in the

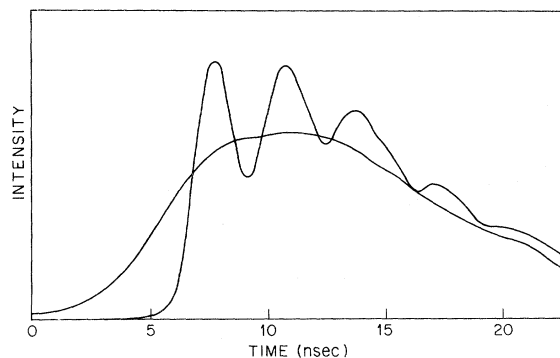


FIG. 20. Multiple pulse breakup in a 1-cm-long cell with similar optics as explained for Fig. 3. The longer input pulse permits indications of breakup into five output pulses. The input was probably slightly larger than shown since the output breakup usually caused oscillations about the input.

same way as shown in Fig. 3.

When the laser frequency is centered on the Rb absorption, only those atoms moving transverse to the beam are able to absorb the light. The beam could not be much smaller than 100 μm before the transit time of the atoms across the uniform portion of the laser beam would become comparable to the pulse length.

a. Diffraction and stripping. One would expect diffraction effects to become important for a Fresnel number η of order unity ($\eta = R^2/\lambda L$, where R is the limiting radius, λ the wavelength, and L the length). This is about 4 for the 1-mm cell and 0.4 for the 1-cm cell. These numbers could be much smaller in the π region in which only the central portion becomes transparent. Such a stripping away of the less intense edges of a pulse was observed by transverse scans. Gaussian inputs were stripped into almost rectangular output profiles of half the width at half-maximum. One might argue that this stripping effect of SIT is much like inserting apertures which reduce the diffraction losses.²⁶ The length for calculating the the Fresnel number may then be α^{-1} yielding $\eta = 20$ and 2 for $\alpha L = 5$ and $L = 0.1$ and 1 cm, respectively. In any case the results in the 1-cm cell corroborate the results of Fig. 3 and indicate the absence of any substantial degradation of the pulse shapes in that figure resulting from diffraction, except perhaps in the π region.

b. Focusing and defocusing. McCall and Hahn² point out that focusing (blooming) can occur if the applied frequency is on the high- (low-) frequency side of the resonance line. A quantitative estimate of these efforts can be made starting with their² Eq. (57) for the phase shift for a 2π sech pulse $\mathcal{E}(z, t) = (2/\kappa\tau) \text{sech}[(1/\tau)(t - z/V)]$:

$$\begin{aligned} \frac{d\varphi(z)}{dz} &= k' \\ &= \frac{\alpha\tau^2}{2\pi g(0)} \int_{-\infty}^{\infty} g(\omega_0 - \omega') \\ &\quad \times \left(\frac{\omega' - \omega}{1 + (\omega' - \omega)^2\tau^2} \right) d(\omega' - \omega), \quad (33) \end{aligned}$$

with ω_0 the center of the Rb absorption and ω the center of the laser pulse profile. The dispersion function in large parentheses has peak values of $\mp 1/2\tau$ for $\omega' = \omega \mp 1/\tau$. A crude approximation to the integral is found by replacing the dispersion function by a triangular function with zeroes at $\omega' = \omega \mp 2/\tau$ and $\omega' = \omega$ and with values $\mp 1/2\tau$ at $\omega' = \omega \mp 1/\tau$ and by replacing the absorber spectral density function by $g((\omega_0 - \omega) + 1/\tau)$ for $\omega' < \omega$ and $\omega' > \omega$, respectively; i. e.,

$$k(\omega) \approx \frac{\alpha\tau^2}{2\pi g(0)} \left(\frac{-1}{2\tau^2} \right) \left[g\left((\omega_0 - \omega) + \frac{1}{\tau} \right) \right.$$

$$\left. - g\left((\omega_0 - \omega) - \frac{1}{\tau} \right) \right] \quad (34a)$$

$$\approx \frac{\alpha}{\pi} \left[\frac{(\omega_0 - \omega)\beta^2}{\tau} \right] e^{-\beta^2(\omega_0 - \omega)^2}, \quad (34b)$$

where $\beta = (\ln 2)^{1/2}/\pi\Delta\nu_D$, and $\Delta\nu_D$ is the full width at half-maximum Doppler width. Equation (34b) was obtained by expanding $g((\omega_0 - \omega) \pm 1/\tau) = g(0)e^{-\beta^2((\omega_0 - \omega) \pm 1/\tau)^2}$ in powers of β/τ . The phase shift φ over a distance L may now be estimated. Assume $\alpha L = 20$ as the largest reasonable absorption and choose $\omega_0 - \omega = -2\pi\Delta\nu_D$ for which φ is approximately maximum. Then with $\Delta\nu_D = 0.55$ GHz for ^{87}Rb , $\varphi = kL = -0.32/\tau$ with τ in nanoseconds. For an input Gaussian transverse spatial profile, the phase difference between a 2π input intensity from the center of the profile and a π input intensity from the edges is then $\Delta\varphi = -0.032$ if $\tau = 5$ nsec for the 2π output pulse and 10 nsec for the π output pulse. So for the laser frequency above the absorption center the central portion lags behind the outer portions and focusing occurs. But the focusing in this example is weak: The change in distance is $\Delta l = \Delta\varphi\lambda/2\pi \approx -0.004$ μm . If the π intensity occurs at a radius of 40 μm from the profile center the focusing angle is 10^{-4} , i. e., the focal length would be about 40 cm. Presumably this focusing and the corresponding defocusing for the laser frequency below resonance could be observed. But focusing and defocusing were unimportant in the experiment summarized in Sec. IV A5, where $|\omega_0 - \omega| \leq 2\pi\Delta\nu_D/10$ and $\alpha L \approx 5$ (yielding a focal length of 1600 cm or more by the above estimate).

Consistent with the lack of any important adverse transverse effects, there was no evidence for the formation of filaments as reported in Ref. 2.

B. Off-Resonance Plane-Wave Case

The experimental results of Sec. IV A were all for the case of the laser frequency equal (within $\Delta\nu_D/10$) to the center frequency of the inhomogeneous absorption profile of width $\Delta\nu_D$. It was simple to increase or decrease the magnetic field to study SIT off resonance. Careful pulse shape and non-linear transmission data were not taken and compared with theory. But qualitatively the pulse shapes off resonance were identical to those on resonance provided the density was increased to give the same αL off resonance. In other words, the pulse shapes changed with αL by tuning off resonance in the same manner as when αL is changed on resonance by varying the temperature.

1. Focusing

No focusing or defocusing effects as discussed in Sec. IV A 7 (b) were observed even though the region of maximum effect was scanned. However for αL

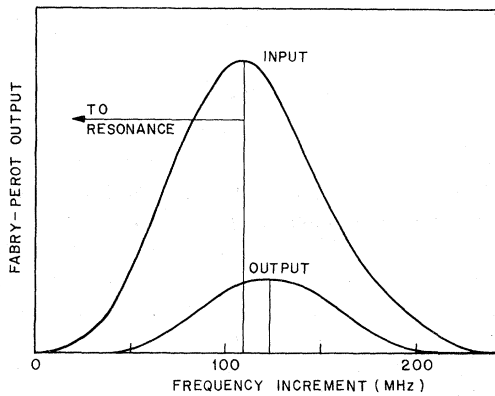


FIG. 21. Frequency shift away from the center of the absorption resonance at low input intensities. The laser frequency was about 0.7 GHz above the center of the 0.55-GHz wide absorption profile. The output was integrated almost three times as long as the input. αL at the laser frequency was roughly 7.

≈ 5 the focal length from Sec. IV A 7 (b) should have been about 160 cm which would have been difficult to detect with the shorter focal-length optics used. Certainly focusing and defocusing effects were small under the conditions of this experiment and rather than being a problem they would require careful measurements to be seen at all.

2. Frequency Shifting

The question arises to the stability of off-resonance SIT pulse propagation. Diels has treated this case numerically assuming a Lorentzian absorption profile of width 0.1 GHz centered 0.2 GHz above the laser frequency.²⁷ He found that a 2π sech input pulse propagates with no change in shape or frequency as shown analytically by McCall and Hahn. But a sech input pulse of width 8 nsec and area of 1.6π was pulled toward the transition frequency by 0.02 GHz while the area reshaped to a 2π sech output pulse. An on resonance αL of about 34 was required for this reshaping corresponding to an αL of about 2 at the laser frequency. Thus Diels's computer solution is in agreement with the observation mentioned above that reshaping occurs at about the same rate on and off resonance for the same αL . Diels's computer calculation yielded a shift of 10% of the laser-absorber frequency difference with the input pulse profile spanning about 20% of that difference (assuming his 8 nsec is the FWHM) and 40% of the linewidth. In the Rb system, a 5-nsec pulse spans only about 15% of the linewidth. One would then expect the frequency pulling to be less since there is less change in αL across the pulse profile.

A search for frequency shifts was made using the Fabry-Perot described in Sec. III A 3. A PAR 160 boxcar and PDP-8 data averager were used to in-

tegrate the short Fabry-Perot output pulses to improve the signal-to-noise ratio. The integration was limited to a few minutes by slow drifts of the Fabry-Perot spacing and the laser frequency. The Fabry-Perot instrument function had a FWHM of about 25–30 MHz with 3000-MHz free spectral range as determined with the 1- μ sec-long laser pulse. Frequency shifts of 5 or 10 MHz of the output relative to the ≈ 100 -MHz-wide input profile could have been seen. No pulling toward the resonance was observed over a wide range of input areas ($\approx \pi$ – 3π) and αL 's (3–10) and out to two Doppler widths below the lower ^{87}Rb resonance or above the upper one.

Two effects were observed however. First, at the lowest input areas around π a shift was seen as much as 10 or 20 MHz *away* from the resonance with the laser frequency about a Doppler width above or below the transition frequency (see Fig. 21). This shift away from resonance is expected at low intensities as a consequence of the higher absorption coefficient for those Fourier frequency components of the pulse closer to resonance. It is interesting that Diels's numerical solution shows a shift away from resonance in the first 10% of the sample length, probably because a thin sample absorbs more of the frequency components close to resonance but is too weak to appreciably reshape the pulse. At greater sample lengths reshaping becomes more important; since there are more atoms closer to resonance taking part in the reshaping it is plausible that the pulse center frequency shifts toward the resonance center. But in the Rb experiment only the linear shift away from center was observed. The absence of experimental shifts damped out the intention to study them numerically. A shift of 2% of the absorption width could have been detected compared with the 10% shift in Diels's numerical solution. Presumably, the smaller ratio of pulse frequency width to absorption width and perhaps the Doppler rather than Lorentzian profile account for the unimportance of frequency pulling in the Rb case.

The second interesting observation was the change in pulse frequency profile as a result of SIT reshaping. A 2π pulse changes shape very little in either the time or frequency domain. But a 3π pulse is narrowed (broadened) in the time (frequency) domain and conversely for a π input pulse as shown in Fig. 22.

3. Chirping

That the output pulse profile appeared as the Fourier transform convolved with the Fabry-Perot instrument function is taken as a convincing demonstration of the absence of large chirps introduced by SIT. Such convolutions were not carried out with precision, but any chirp would have to be

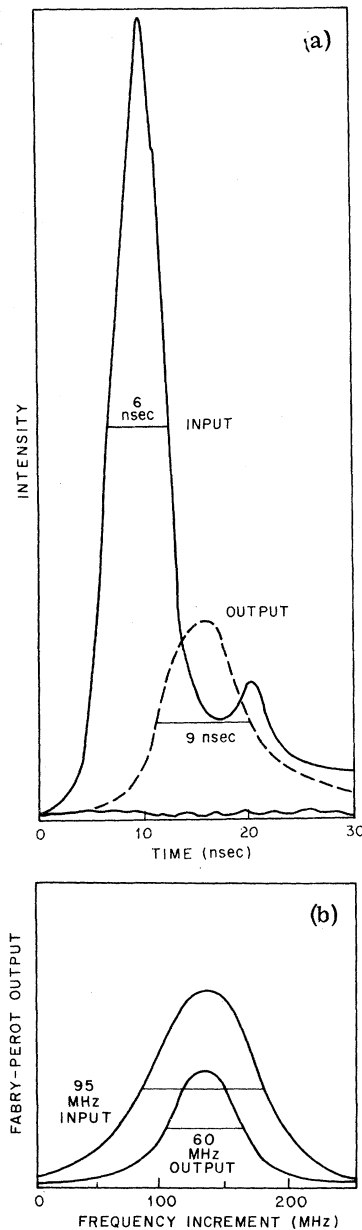


FIG. 22. SIT lengthening of a $\approx \pi$ pulse in the time domain (a) accompanied by narrowing in the frequency domain (b). The output in (c) was integrated $\frac{5}{3}$ as long as the input.

small compared with the frequency width. The lack of any noticeable change in profile for a 2π input pulse would be inconsistent with a chirp of more than 10 MHz for the duration of the pulse. Davidovich and Eberly⁹ have invoked the possibility of chirping to explain the difference between their very short preferred-pulse-width SIT pulses and the Hg-Rb results, but they have given no estimate of the magnitude of the hypothetical chirps. The slowly varying envelope approximation leads to Eqs. (19)-

(22) and (9) without the \dot{u} term, the numerical solutions of which are in excellent agreement with experimental results as discussed in Sec. IV A. Chirps were not permitted in the calculations and did not appear in the observations to the accuracy stated above. In Appendix A it is shown that the terms usually discarded, but retained by Davidovich and Eberly in Eqs. (9) and (10), are negligible for the Hg-Rb system and may be masked by effects caused by nonresonant levels.

C. Pulse Shortening with a Uniform Spherical Wave

In Secs. IV A 3 and IV A 4 it was shown that a uniform-plane-wave input pulse with area just under 3π is reshaped by SIT into a propagating pulse of area 2π with its peak amplified and its width narrowed relative to the input pulse. With lenses the output 2π pulse could be spatially compressed to increase its intensity to 3π ; further compression and amplification could then be achieved in a second sample, etc. This sequential scheme is approximated crudely by focusing the input through a single absorption cell with a simple lens. A compression of an order of magnitude has been reported by this technique.²⁸ A 1.3-cm focal-length lens focused the 0.8-mm-diam laser beam through a ⁸⁷Rb absorption cell of length $L = 5$ mm; see Fig. 23(a). The unchirped 10-nsec input pulse was the single-pass transmission of the 1- μ sec laser pulse through the Pockels-cell shutter. A Sylvania 502 GaAs crossed-field photomultiplier and 75-psec rise-time Tektronix sampling oscilloscope provided fast detection (see Sec. III C). The results are shown in Fig. 23(b) in which each trace was obtained by 30-sec sweeps of the sampling gate corresponding to about 5000 distinct input pulses.

A computer simulation of this pulse compression was made in which Eq. (9) was replaced by

$$\frac{\partial \mathcal{E}}{\partial r} + \frac{1}{c} \frac{\partial \mathcal{E}}{\partial t} = -\frac{\mathcal{E}}{r} - \frac{2\pi\omega}{c} \int_{-\infty}^{+\infty} g(\Delta\omega) v(r, t, \Delta\omega) d(\Delta\omega) \quad (35)$$

for an incoming uniform spherical wave, where r is the radial distance from the focal point. The agreement between the calculations and data shown in Fig. 23 is excellent considering the averaging effects of diffraction and limited time response and stability.

A simple argument favoring the geometry of Fig. 23 is as follows: An input pulse of area A equal to 3π loses an area of π while being reshaped into a 2π pulse in a reshaping length $L_R = R/\alpha$, where R is typically 3-5:

$$\left. \frac{\partial A}{\partial r} \right|_{\text{SIT}} \approx -\frac{A}{3L_R} \quad (36)$$

Reshaping, and hence amplification and compression, will continue throughout the absorber if this

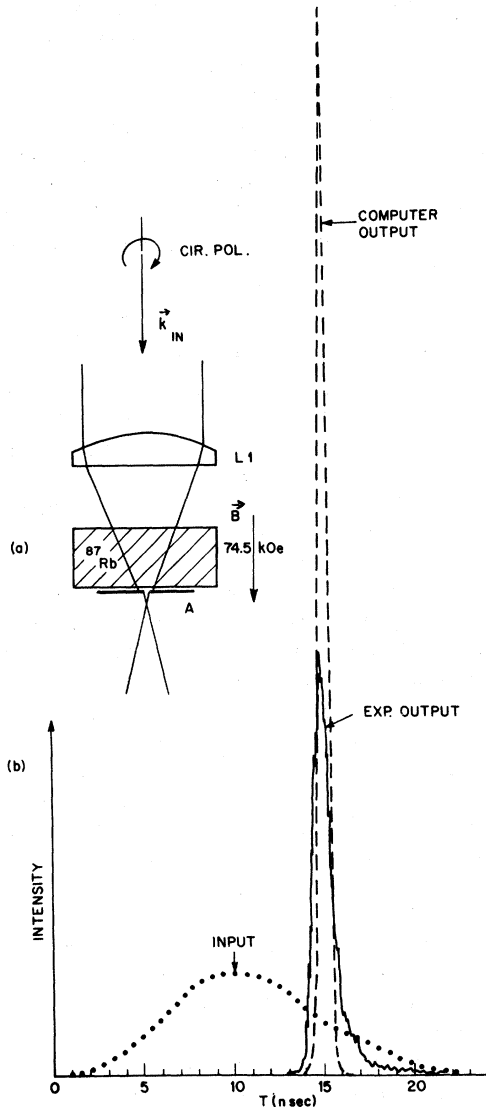


FIG. 23. Optical-pulse compression by focusing. (a) Optical-pulse compressor. L1 is a 13-mm minimum aberration single-element lens. The top and bottom of the absorption cell were about 6.6 and 1.6 mm above the focal point, respectively. The aperture A shown at the cell exit was, in fact, a 25- μ m aperture placed at the image plane of an output magnifying telescope consisting of 2.5- and 31-cm lenses. (b) Comparison of experimental data with computer simulation. The solid and dashed curves are the experimental and theoretical output pulses with $\alpha L \approx 25$ as viewed through the 25- μ m aperture. The dotted curve is the pulse detected through the aperture with $\alpha L \approx 0$ (obtained simply by converting the input polarization from absorbable right-circularly polarized to unabsorbable left-circularly polarized light). The input pulse area of 3.5π assumed in the uniform-profile computer calculation agrees well with the experimental calibration of the area by SIT without focusing. In the computer calculation the pulse intensity is assumed to increase by focusing as the inverse square of the distance to the theoretical focal point. The inclusion of diffraction, laser amplitude fluctuations, and time jitter would broaden and attenuate the computer output pulse.

reshaping loss is offset by a gain $A/3L_R$. Or since $A = (2p/\hbar) \int_{-\infty}^{\infty} \mathcal{E}(t) dt$,

$$\left. \frac{\partial \mathcal{E}}{\partial r} \right|_{\text{gain}} \approx \frac{\mathcal{E}}{3L_R} \quad (37)$$

But from Eq. (35) the gain from a single simple lens is \mathcal{E}/r . So optimum compression occurs when r is approximately constant and equal to $3L_R$. The cell was placed as shown in Fig. 23 to approximate $r \approx 3L_R$. Inclusion of the focal region within the cell increased the transmission but reduced the compression because the gain in pulse area by focusing was much greater than the loss by reshaping.

The actual input area in Fig. 23 was probably somewhat over 3π ; with an αL of 25 any small second pulse is greatly attenuated. But for higher intensities breakup into two well-separated pulses can be seen as shown in Fig. 24.

Since the 0.55 GHz ^{87}Rb Doppler absorption width is little larger than the spectral width of the compressed pulse $\approx (\pi\tau_p)^{-1} \approx 0.3$ GHz, the question arises whether the compression is limited by the absorption width. In Sec. IIIB1 and Fig. 11 it was shown that the ^{85}Rb absorption at 74.5 kOe is inhomogeneous and almost uniform over 3 GHz. Experimental and computer comparisons of both ^{85}Rb and ^{87}Rb showed little difference in their effectiveness in

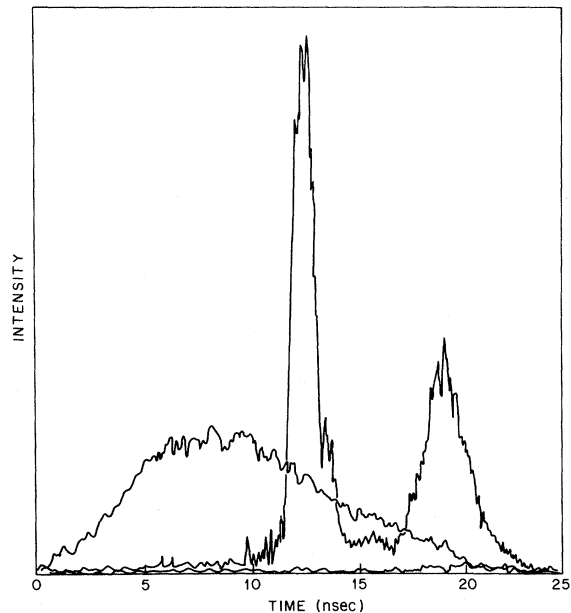


FIG. 24. Pulse breakup of a uniform spherical wave into two well-separated pulses. Conditions were similar to those of Fig. 23 except for slightly higher αL , and of course, higher input intensity. The compensation of losses by focusing permits a high αL , and hence good pulse separation, without excessive reduction in the transmission.

compressing the 10-nsec input pulses. Presumably ^{85}Rb would be preferred for 1-nsec input pulses however.

V. SUMMARY

The ideal conditions for observing the important features of self-induced transparency as predicted by McCall and Hahn have been shown to be closely approximated by the Hg-Rb system. Excellent agreement between computer simulation and actual observation was obtained for the following interesting features: nonlinear transmission, large delays, pulse breakup, and peak amplification of a uniform plane wave and time compression of a uniform spherical wave. These basic characteristics of SIT were shown to be much more important than focusing, defocusing, or frequency shifting, or chirping even off resonance. The terms in Maxwell's equations (9) and (10) retained by Davidovich and Eberly in their preferred-width pulse theory were shown to be negligible over the times of the present experiment, consistent with the excellent agreement between data and the theory of McCall and Hahn.

Possible extensions of this work include pulse compression in the picosecond regime, SIT in homogeneously broadened absorbers, investigations of ways to approximate the nondegeneracy and uniform-plane-wave conditions more easily in a greater number of systems, and development of SIT optical integrated circuit delay and compression components.

ACKNOWLEDGMENTS

The authors are grateful to I. Asher, J. H. Eberly, S. L. McCall, and M. O. Scully for helpful discussions, to J. H. Eberly and S. L. McCall for critical reading of the manuscript, to M. A. Duguay for the use of a Pockels cell, to T. S. Kinsel for the use of a crossed-field photomultiplier, and to M. V. Schneider for preparing the thin-film single-mode selector.

APPENDIX A: PREFERRED-WIDTH REGIME

Davidovich and Eberly (DE) retain the \dot{u} term in Eq. (9) and the \mathcal{E}'' , $\dot{\mathcal{E}}$, and \dot{v} terms in Eq. (10).⁹ They assume that $\partial\Phi/\partial t = 0$ so that four of their equations look like Eqs. (22) and (24)–(26) of McCall and Hahn.^{2b} They then find the McCall and Hahn equations (42) and (52)–(54) still to be the solutions for \mathcal{E} , u , v , and W . Then by substitution in their original equations and assuming a Lorentzian spectral profile $g(\Delta\omega)$ they obtain values of the pulse velocity V , field \mathcal{E} , pulse width τ , and linear phase shift $\Delta k = \Phi' = \partial\Phi/\partial z$ as a function of the atomic parameters. In the DE solutions there are sech^3 and sech terms in the second wave equation; equating of the coefficients of the sech^3 and sech terms to zero fixes both V and τ . On resonance for Rb they

find $V = \frac{1}{3}$ and $\tau \approx 0.1$ nsec. Why are these values so different from the values $V = c/1000$ and $\tau \approx 10$ nsec found experimentally? DE attribute this difference to chirping in the experimental pulse.⁹

The various terms in the wave equations are evaluated crudely in Table II for the conditions of the present Rb experiment and for the parameters of the DE solution. In the first equation shown in column (a), the \mathcal{E}' , $\dot{\mathcal{E}}$, and $\omega^2 v$ terms dominate in both cases since Φ'/k and $\dot{\Phi}/\omega$ are less than 10^{-4} even off resonance. It is the second wave equation of column (a') which leads to the preferred-width results. For on-resonance calculations [$g(\omega)$ maximum for $\omega = \omega_0$], this equation has been neglected entirely as in the simulation of the Rb experiment [symmetric $g(\omega)$ is assumed]. This appears justified because all of the terms are small relative to the terms driving \mathcal{E} in the first wave equation. For example, $\Delta\mathcal{E}/\mathcal{E} \approx \frac{1}{4}$ in a time τ from the $\omega^2 v$ term of (a) but $\Delta\mathcal{E}/\mathcal{E} \approx 10^{-3}$ if $\mathcal{E}'' = -(8\pi/c^2)[g\omega\dot{v}]$ in (b'). However, DE do have a point in that this equation must be satisfied. How is this done without making V large so that the sech^3 part of the \mathcal{E}'' term is as small as the $\omega\dot{v}$ term? From the numerical estimates given in (b'), it is apparent that the \mathcal{E}'' term is not offset by unchirped on-resonance terms.

Then how large a phase shift would be necessary to satisfy (a')? The $\dot{\Phi}\mathcal{E}$ term cancels the \mathcal{E}'' term for $\dot{\Phi}/\omega \approx 10^{-10}$ or a net chirp over the pulse of less than 50 kHz or a phase shift of about 2 mrad. Alternatively $\Phi'/k \approx 10^{-9}$ or a phase shift of 0.01 mrad would suffice. This would require that the $\dot{\Phi}\mathcal{E}$ and $\Phi'\mathcal{E}$ terms have sech^3 components, i. e., $\dot{\Phi}$ and Φ' must have sech^2 components. So although (a') must be satisfied, this might occur in a number of different ways not all of which include chirps. Thus the chirp required to satisfy the second wave equation would have been much too small to have been observed in the Rb experiment. If the laser-absorber coincidence were stable to a few Hz and if spontaneous emission losses could be eliminated and if no other terms such as from other transitions or chirping were important, then in a sample length of several hundred absorption lengths (α^{-1}) the pulse might evolve to the preferred width and velocity. But for practical conditions the SIT features discussed in Secs. IV A 1–IV A 5 (which occur in the first few absorption lengths) would proceed with no need for the DE solution to explain them.

Are there other experimentally realizable conditions under which the DE approach is essential for a correct treatment? When the input pulse width is in the neighborhood of the DE preferred width, the terms retained by DE can no longer be disregarded. For example, if a 0.1-nsec input pulse were incident on ^{87}Rb , then $\Delta\mathcal{E}/\mathcal{E} \approx 1$ from the $\omega^2 v$ term of (a) in Table II and $\Delta\mathcal{E}/\mathcal{E} \approx 1$ from the on-resonance $\omega\dot{v}$ term of (a'). That is, both wave

TABLE II. Approximate values of the various terms in the wave equations. The terms of the two equations are listed in columns (a) and (a'). In columns (b) and (b'), numerical values of the terms are given for the present Rb experiment with the following approximations. A traveling wave solution is assumed; $\partial/\partial z = -(1/V)\partial/\partial t \approx -1/V\tau$ with $V=c/1000$ and $\tau \approx 10^{-8}$. The value of \mathcal{G} is assumed to satisfy $\kappa\mathcal{G}\tau \approx 2\pi$, $\kappa = 8 \times 10^9$. The integrals over the spectral profile $g(\Delta\omega)$ are approximated by $\int g(\Delta\omega)f(\Delta\omega) d(\Delta\omega) \approx g(0)f(0)$ for symmetric $f(\Delta\omega)$ and $[g(0)f(0)/\tau] [\delta\omega/(1/\tau)]$ for asymmetric $f(\Delta\omega)$ where $f(\Delta\omega)$ has width $\approx 1/\tau$; $g(0) = 0.27 \times 10^{-9}$ from the Doppler profile. Finally $u(0) = v(0) = N\rho \approx 4 \times 10^{-6}$. All units are cgs. The terms included by McCall and Hahn and by Gibbs and Slusher are underlined. In columns (c) and (c') a similar evaluation of the terms is given for the Davidovich and Eberly solution: $V = \frac{1}{3}c$, $\tau \approx 10^{-10}$; they included the underlined terms in their analytic solution. The $\tau\delta\omega$ terms vanish on resonance and $\delta\omega \leq 1/\tau$. The $\dot{\Phi}$ and $\dot{\Phi}'$ terms are difficult to evaluate; usually $\dot{\Phi} = \partial\Phi/\partial t$ is assumed zero to eliminate $\dot{\Phi}$ terms in the Bloch equation.

(a)	(b)	(c)	(a')	(b')	(c')
$-2k\mathcal{G}'$	10^4	6×10^5	\mathcal{G}''	10^{-1}	<u>10</u>
$-2\dot{\Phi}'\mathcal{G}'$	$10^4\dot{\Phi}'/k$	$10^6\dot{\Phi}'/k$	$-\frac{n^2}{c^2}\dot{\mathcal{G}}$	10^{-6}	<u>1</u>
$-2\frac{\eta^2}{c^2}\omega\dot{\mathcal{G}}$	<u>10^2</u>	<u>4×10^5</u>	$-2k\dot{\Phi}'\mathcal{G}$	$10^8\dot{\Phi}'/k$	<u>$10^{10}\dot{\Phi}'/k$</u>
$+2\frac{\eta^2}{c^2}\dot{\Phi}\dot{\mathcal{G}}$	$10^2\dot{\Phi}/\omega$	$10^6\dot{\Phi}/\omega$	$-(\dot{\Phi}')^2\dot{\mathcal{G}}$	$10^9(\dot{\Phi}'/k)^2$	$10^{11}(\dot{\Phi}'/k)^2$
$-\mathcal{G}\Phi''$	$10^9\Phi''/k^2$	$10^{11}\Phi''/k^2$			
$+\eta^2\mathcal{G}\ddot{\Phi}/c^2$	$10^9\ddot{\Phi}/\omega^2$	$10^{11}\ddot{\Phi}/\omega^2$	$-2\frac{\eta}{c^2}\omega\dot{\Phi}\dot{\mathcal{G}}$	$10^9\dot{\Phi}/\omega$	$10^{11}\dot{\Phi}/\omega$
$= -\frac{4\pi}{c^2}\int g u \ddot{\Phi}$	$10^4\dot{\Phi}/\omega^2$	$10^6\dot{\Phi}/\omega^2$	$+\frac{\eta^2}{c^2}(\dot{\Phi})^2\mathcal{G}$	$10^9(\dot{\Phi}/\omega)^2$	$10^{11}(\dot{\Phi}/\omega)^2$
$+\frac{4\pi}{c^2}\int g \dot{v}$	10^{-11}	10^{-5}	$= \frac{4\pi}{c^2}\int g \dot{u}$	$10^{-11}\tau\delta\omega$	$10^{-5}\tau\delta\omega$
$+\frac{8\pi}{c^2}\int g \omega \dot{u}$	$10^{-3}\tau\delta\omega$	$10\tau\delta\omega$	$-\frac{8\pi}{c^2}\int g \omega \dot{v}$	10^{-3}	<u>10</u>
$-\frac{8\pi}{c^2}\int g \dot{\Phi} \dot{u}$	$10^{-3}(\dot{\Phi}/\omega)(\tau\delta\omega)$	$10(\dot{\Phi}/\omega)(\tau\delta\omega)$	$+\frac{8\pi}{c^2}\int g \dot{\Phi} \dot{v}$	$10^{-3}\dot{\Phi}/\omega$	$10\dot{\Phi}/\omega$
$-\frac{4\pi}{c^2}\int g \omega^2 v$	<u>10^4</u>	<u>10^6</u>	$-\frac{4\pi}{c^2}\int g \omega^2 u$	<u>$10^4\tau\delta\omega$</u>	<u>$10^6\tau\delta\omega$</u>
$+\frac{8\pi}{c^2}\int g \omega \dot{\Phi} v$	$10^2\dot{\Phi}/\omega$	$10^4\dot{\Phi}/\omega$	$+\frac{8\pi}{c^2}\int g \omega \dot{\Phi} u$	$10^4(\dot{\Phi}/\omega)(\tau\delta\omega)$	$10^6(\dot{\Phi}/\omega)(\tau\delta\omega)$
$-\frac{4\pi}{c^2}\int g \dot{\Phi}^2 v$	$10^4(\dot{\Phi}/\omega)^2$	$10^6(\dot{\Phi}/\omega)^2$	$-\frac{4\pi}{c^2}\int g (\dot{\Phi})^2 u$	$10^4(\dot{\Phi}/\omega)^2(\tau\delta\omega)$	$10^6(\dot{\Phi}/\omega)^2(\tau\delta\omega)$
			$+\frac{4\pi}{c^2}\int g v \ddot{\Phi}$	$10^4\ddot{\Phi}/\omega^2$	$10^6\ddot{\Phi}/\omega^2$

equations contribute about equally to changes in \mathcal{G} , and both would have to be included in a correct theoretical calculation even on resonance (assuming *no* relaxation, *no* off-resonance levels, and *no* backward traveling wave introduce dominating terms or destroy the independence of the two wave equations).

The 0.1-nsec Rb experiment would still not be easy to accomplish under the DE assumptions. For exact resonance with two levels and $\dot{\Phi} = 0$, the inevitable presence of other electric dipole transitions in real systems can easily contribute more to the second equation (a') than the DE terms. Off-resonance transitions can be divided into two classes: (I) those with the same lower level as the resonant transition and (II) those from other occupied lower levels. For Rb the most important class II transitions are the D_1 transitions from the other three M_J levels (see Fig. 9). The DE term $\int g \omega \dot{v}_R$ is approximately $g(0)\omega v_R/\tau^2$ where $v_R \propto N_R \rho_R$ is the on-resonance polarization. The $\omega^2 u$ term, which vanishes by symmetry for the resonant transition, is

non-negligible for off-resonant polarizations u_{NR} . In the rotating frame the polarization adiabatically follows the effective electric field far off resonance, so $u_{NR} \approx N_{NR} \dot{\rho}_{NR}/\tau\Delta\omega$ [Eq. (52) of Ref. 2b]. Assuming $\Delta\omega$ is almost constant over the nonresonant spectral profile $g_{NR}(\Delta\omega)$ of width δ , one has

$$\int g_{NR} \omega^2 u_{NR} d(\Delta\omega) \approx g_{NR}(0) \omega^2 v_R \delta / \tau \omega_{OR}, \quad (A1)$$

where ω_{OR} is frequency difference between the two transitions. The ratio of the $\omega^2 u_{NR}$ term to the $\omega \dot{v}_R$ term is then

$$\approx \frac{g_{NR}(0)}{g_R(0)} \frac{\delta}{\omega_{OR}} \frac{N_{NR} \dot{\rho}_{NR}}{N_R \rho_R} \omega \tau. \quad (A2)$$

For ^{87}Rb this reduces to $\omega\tau\delta/\omega_{OR} \approx 6 \times 10^6$ with $\delta \approx 0.56$ GHz, $\omega_{OR} \approx 1.9$ GHz, and $\tau = 10$ nsec. For the present experiment the $\omega^2 u_{NR}$ term still introduces only a slight linear phase shift. The large ratio of the $\omega^2 u$ term to the DE term would not change the DE analysis. It appears that the $\omega^2 u_{NR}$ term in the DE analysis results in $\Delta k \neq 0$, $V \approx \frac{1}{3}c$, and a different preferred width.

The largest class I transition in ^{87}Rb is the $D_2(^2S_{1/2}$ to $^2P_{3/2})$ line of the same m_I . The lower level of the off-resonance transition is emptied and refilled by the action of the \mathcal{E} field on the resonant transition. The off-resonance polarization is then unable to adiabatically follow the effective electric field since it is modulated by the effect of the on-resonance polarization. The $\omega^2 u_{NR}$ term may then contribute sech^3 terms which would change the $V \approx \frac{1}{2}c$ of DE. The ratio of the magnitudes of the $\omega^2 u_{NR}$ and $\omega \dot{v}_R$ terms is again approximated by Eq. (A2). For the D lines in ^{87}Rb , the ratio is about 100 with $\delta \approx 0.56$ GHz, $\omega_{0R} \approx 238$ cm^{-1} , and $\tau = 10$ nsec. In this case, it is quite likely that the DE analysis is inappropriate and that the off-resonant transitions would contribute much more to the evolution of the pulse envelope than the DE term. It is difficult to conceive of a real atom where this would not be the case.

In conclusion, it has been shown that the DE prediction of a preferred width and velocity does not invalidate the good agreement between the present experimental results and the usual theory of SIT based on the neglect of the second wave equation. Evolution toward the DE preferred values is undoubtedly quite slow. Spontaneous emission damping would ordinarily destroy the pulse long before the preferred values were attained, unless the input pulse was very nearly the preferred pulse itself. Even so, other electric dipole transitions, which are always present, introduce terms much larger than those included by DE. Even if one granted the other assumptions of DE, the $\dot{\Phi} = 0$ assumption would still be suspect. The stability of the preferred solution should be examined by solving the set of five simultaneous equations with u , v , W , \mathcal{E} , and Φ all being functions of $\Delta\omega$, z , and t . Laboratory systems also have incoherent damping, inhomogeneities, and particle velocity effects which may affect the propagation more than the second wave equation. The pulse evolution in a real absorbing system in the picosecond regime is now under study.

APPENDIX B: BLOCH'S EQUATIONS FOR SPONTANEOUS EMISSION

Several theoretical treatments^{2,10} of SIT have included damping caused by incoherent-decay processes. However, previous inclusions of the transverse (decay of u and v) and longitudinal (decay of W) decay times, T_2' and T_1 , respectively, do not specify how they are evaluated for spontaneous radiation between states of a two-level atom. In addition, for the Rb atom in a magnetic field studied here, the excited state also decays spontaneously to a third level. Decay from the third level back to the ground state is very slow compared to the nanosecond time scale of the SIT experiment, so

that atoms decaying to the third level are lost from the excited two-level system. This third-level loss is small for Rb (effects on the SIT pulse shapes are only a few percent), but it has been included in the computer solutions for accuracy and completeness. In this Appendix the spontaneous decay is included correctly into Bloch's equations, and a fourth equation is added to account for losses to the third level. Effects caused by radiation trapping are not included because they are difficult and geometry dependent and are expected to be small for the densities used in these experiments ($n \approx 10^{10}$ – 10^{12} cm^{-3}). Radiation trapping may be quite important for densities above 10^{14} cm^{-3} and their effect on SIT might be quite interesting.

The theoretical treatment of a damped driven two-level atom by Mollow and Miller²⁹ is followed here. Their treatment correctly includes spontaneous decay between states of a two-level system. In terms of the usual density-matrix notation their Eqs. (2.42) and (2.43) give

$$\dot{\rho}_{aa} = -K\rho_{aa}, \quad (\text{B1})$$

$$\dot{\rho}_{bb} = K\rho_{aa}, \quad (\text{B2})$$

$$\dot{\rho}_{ab} = -\frac{1}{2}K\rho_{ab}, \quad (\text{B3})$$

where

$$K = 1/\tau_{ab}. \quad (\text{B4})$$

Next, to include loss from the excited state to the third level, one can follow Hopf and Scully,¹⁰ who treat losses from both ground and excited state to other states. For Rb using their notation we have

$$\gamma_a = 1/\tau_{ac}, \quad \gamma_b = 0, \quad (\text{B5})$$

$$\gamma_{ab} = \frac{1}{2}(\gamma_a + \gamma_b) = \frac{1}{2}\gamma_a. \quad (\text{B6})$$

Now, using the Bloch equation notation,

$$\langle \sigma_z \rangle = \rho_{aa} - \rho_{bb} = 2W/N\hbar\omega_0, \quad (\text{B7})$$

$$\langle \sigma_x \rangle = \rho_{ab} + \rho_{ba} = 2u/Np, \quad (\text{B8})$$

$$\langle \sigma_y \rangle = i(\rho_{ab} - \rho_{ba}) = 2v/Np, \quad (\text{B9})$$

one obtains [with Eqs.(1.10a)–(1.10d) of Ref. 10b and Eqs. (B1)–(B3) above] the following Bloch equations:

$$\dot{u} = +v\Delta\omega - (\gamma_a + K)\frac{1}{2}u, \quad (\text{B10})$$

$$\dot{v} = -u\Delta\omega - (\gamma_a + K)\frac{v}{2} - \frac{\kappa^2 \mathcal{E}}{\omega} W, \quad (\text{B11})$$

$$\dot{W} = v\mathcal{E}\omega - (\frac{1}{2}\gamma_a + K)(x + W), \quad (\text{B12})$$

$$\dot{x} = -\frac{1}{2}\gamma_a(x + W), \quad (\text{B13})$$

where x is defined as

$$x = \frac{1}{2}N\hbar\omega_0(\rho_{aa} + \rho_{bb}). \quad (\text{B14})$$

The transverse and longitudinal relaxation are now identified as

$$\frac{1}{T_1} = \frac{\gamma_a + K}{2} = \frac{1}{2\tau_{ac}} + \frac{1}{\tau_{ab}}, \quad (\text{B15})$$

$$\frac{1}{T_2} = \frac{\gamma_a + K}{2} = \frac{1}{2\tau_{ac}} + \frac{1}{2\tau_{ab}}; \quad (\text{B16})$$

for Rb, $\tau_{ac} = 84$ nsec, $\tau_{ab} = 42$ nsec, $T_1 = 33.6$ nsec, and $T_2' = 56$ nsec. The Bloch equations in terms of T_1 and T_2' are shown in Eq. (19)–(22).

APPENDIX C: COMPARISON OF KERR- AND POCKELS-CELL SHUTTERS AND PHASE STABILITY OF THE OPTICAL PULSE

That a Kerr cell does and a Pockels cell does not introduce a time-varying phase shift on the short output pulse can be seen as follows. Let the linearly polarized laser pulse be represented by

$$\vec{E} = \mathcal{E}_0(t) (\hat{x} + \hat{y}) 2^{-1/2} \cos \Theta, \quad (\text{C1})$$

where $\mathcal{E}_0(t)$ is the microsecond scale variation in the laser output and $\Theta = \omega t - kz$. The effect of the Kerr cell is to introduce an additional phase $\frac{2}{3}\varphi(t)$ along the applied field direction \hat{y} and to reduce the \hat{x} phase by $\frac{1}{2}\varphi(t)$ ³⁰:

$$\vec{E}_{\text{KC}} = \frac{\mathcal{E}_0(t)}{\sqrt{2}} [\hat{x} \cos(\Theta - \frac{1}{3}\varphi) + \hat{y} \cos(\Theta + \frac{2}{3}\varphi)]. \quad (\text{C2})$$

The final linear polarizer of the Kerr-cell shutter (KCS) transmits only along $(\hat{x} - \hat{y})/\sqrt{2}$:

$$E_{\text{KCS}} = [(\hat{x} - \hat{y}) \cdot \vec{E}_{\text{KC}}/\sqrt{2}] \quad (\text{C3a})$$

$$= \mathcal{E}_0(t) \sin \frac{1}{2}\varphi(t) \sin[\Theta + \frac{1}{6}\varphi(t)] \quad (\text{C3b})$$

$$= \mathcal{E}_{\text{KCS}}(t) \sin[\Theta + \frac{1}{6}\varphi(t)]. \quad (\text{C3c})$$

Thus, the phase of the Kerr-cell output is time dependent, i. e., it is impossible to choose a frame of reference rotating at a constant angular velocity in which the optical driving field is fixed in direction. Since $\varphi(t)$ varies from zero to π and then back to zero, the direction of \vec{E}_{KCS} changes by 30° and back in the rotating frame. This behavior violates the assumption of no phase variation of Table I (A1).

The Pockels cell introduces a positive phase shift along one axis and a negative one along the other³¹:

$$\vec{E}_{\text{PC}} = \frac{\mathcal{E}_0(t)}{\sqrt{2}} [\hat{x} \cos(\Theta - \frac{1}{2}\beta) + \hat{y} \cos(\Theta + \frac{1}{2}\beta)]. \quad (\text{C4})$$

The Pockels-cell-shutter pulse is then

$$E_{\text{PCS}} = \mathcal{E}_0(t) \sin \frac{1}{2}\beta(t) \sin \Theta \quad (\text{C5a})$$

$$= \mathcal{E}_{\text{PCS}}(t) \sin \Theta; \quad (\text{C5b})$$

i. e., a pulse of constant phase and variable amplitude appearing at rest in the appropriate rotating frame.

The distinction between the Kerr-cell and Pockels-cell pulses was further investigated by mixing each with the long input pulse. The input pulse was converted to the output polarization by two linear po-

larizers. With mirrors and beam splitters it bypassed the Pockels shutter and rejoined the Pockels-cell beam before being mixed by the TIXL59 silicon avalanche photodiode. This different path through air fluctuations, mirror vibrations, etc., introduced a time-varying phase shift $\alpha(t)$ into this reference carrier wave

$$E_c = \mathcal{E}_0(t) \cos(\Theta + \alpha), \quad (\text{C6})$$

where the amplitude is adjusted to equal the peak of E_{KCS} and E_{PCS} . The mixing signals are then

$$\langle |E_c + E_{\text{KCS}}|^2 \rangle_{\text{av}} = \frac{1}{2} \mathcal{E}_0^2 [1 + \sin^2 \frac{1}{2}\varphi - 2 \sin \frac{1}{2}\varphi \sin(\alpha - \frac{1}{6}\varphi)], \quad (\text{C7a})$$

$$\langle |E_c + E_{\text{PCS}}|^2 \rangle_{\text{av}} = \frac{1}{2} \mathcal{E}_0^2 (1 + \sin^2 \frac{1}{2}\beta - 2 \sin \alpha \sin \frac{1}{2}\beta). \quad (\text{C7b})$$

Assume that $\langle E_{\text{PCS}}^2 \rangle_{\text{av}}$ and $\langle E_{\text{KCS}}^2 \rangle_{\text{av}}$ are equal to $\frac{1}{2} \mathcal{E}_0^2 \sin^2 \frac{1}{2}\beta$ and are given by the dashed curves in Fig. 26. The expected signal for various values of the uncontrolled phase α are given in Figs. 25(a) and 25(b) as calculated from Eqs. (C7a) and (C7b). Corresponding experimental mixing signals are shown in Fig. 26. Incomplete mixing prevented

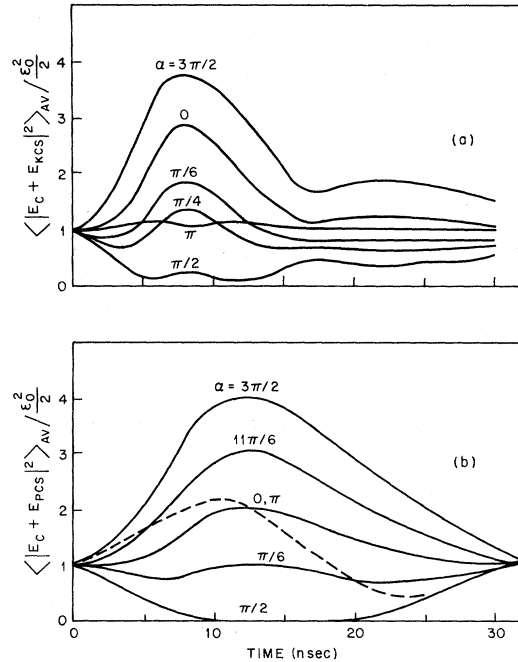


FIG. 25. Calculated mixing of the output pulse from the (a) Kerr-cell and (b) Pockels-cell shutters with the carrier wave of the same frequency but with phase difference α . The shutter input pulses are the dashed curves in Fig. 26. The undesired phase shift in the Kerr-cell pulse gives rise to the higher frequency oscillation in (a) (e.g., $\alpha = \frac{1}{2}\pi$). The dashed curve in (b) is an example of the asymmetry occurring with a linear chirp (of $+\pi$ in the figure).

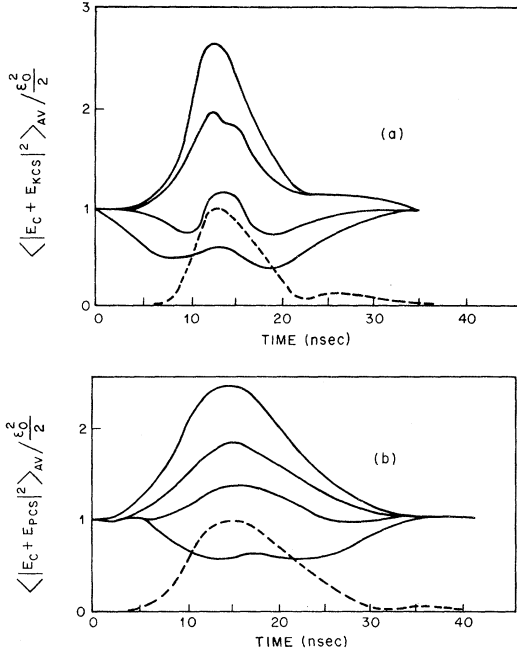


FIG. 26. Experimental mixing of the output pulse from the (a) Kerr-cell and (b) Pockels-cell shutters with the carrier wave of the same frequency but with random phase differences. Comparison with Fig. 25(b) shows that the Pockels-cell output pulse was free of phase shifts. Dashed curves are the experimental inputs.

attainment of a maximum twice the sum of the separate input intensities. However, several conclusions can be drawn. First, an extra oscillation occurs in the Kerr-cell mixing signal for some α 's as anticipated, showing the undesired phase shift. Second, the symmetry in both cases demonstrates that the integrated chirp over the pulse is much less than $1/\tau$. The dashed curve in Fig. 25(b) indicates the effect of a linear chirp from 0 to π over the entire pulse length. Third, the Pockels-cell-shutter optical pulse used in the present SIT experiments was free of significant phase shifts and chirps as required, i. e., $\varphi \ll 1/\tau$.

APPENDIX D: ABSORPTION COEFFICIENT AND ELECTRIC DIPOLE MOMENT

The transition probability per unit time that an atom will absorb a resonance photon of frequency $\nu_0 = (E_a - E_b)/\hbar$ in a transition from ground state b to excited state a is³²

$$R_{ab} = 4\pi^2 e^2 I(\omega) |(r_q)_{ba}|^2 / \hbar^2 c, \quad (D1)$$

where $I(\omega)\Delta\omega$ is the total incident intensity in $\Delta\omega$ and $(r_q)_{ba}$ is the matrix element of the component q of the electron position vector \vec{r} along the direction of polarization of the incident light. Neglecting spontaneous emission back into the beam, one has for the decrease of the intensity in a distance dx

$$-d[I_x(\omega)\delta\omega] = dx R_{ab} \hbar \omega n(\omega) \delta\omega, \quad (D2)$$

where $n(\omega)\delta\omega$ is the density of atoms able to absorb light between ω and $\omega + \delta\omega$.³³ The absorption coefficient $k(\omega)$ is then

$$k(\omega) = -\frac{dI_x(\omega)/dx}{I_x(\omega)} = 4\pi^2 \omega p_0^2 n(\omega) / \hbar c, \quad (D3)$$

where the transition dipole is $p_0 = e |(r_q)_{ba}|$. For a Doppler broadened line

$$n(\omega) = n_b g(\omega) = n_b a \pi^{-1/2} e^{-a^2(\omega - \omega_0)^2}, \quad (D4)$$

where n_b is the density of atoms in the ground state b , $\nu_0 = \omega_0/2\pi$ is the center frequency of the transition, and $a = (\ln 2)^{1/2} \pi \Delta\nu_D$, where $\Delta\nu_D$ is the Doppler width (FWHM).³³ The absorption coefficient α at the center of the line is then

$$\alpha = k(\omega_0) = 8\pi^2 n_b p_0^2 (\pi^{-1} \ln 2)^{1/2} / (\lambda \hbar \Delta\nu_D). \quad (D5)$$

This expression agrees with Eq. (36) of Ref 2(b) if the dipole p_0 is related to the McCall-Hahn dipole p_{MH} by $p_0 = \sqrt{2} p_{MH}$.

The electric dipole moment is found from the measured lifetime τ_a of the upper state and the theoretical expression for spontaneous emission. The total radiative lifetime of the Rb $5p^2P_{1/2}$ excited state has been measured to be 28.1 ± 0.5 nsec.³⁴ The partial lifetime of the $^2P_{1/2}(M_J = +\frac{1}{2}, M_I)$ to $^2S_{1/2}(M_J = -\frac{1}{2}, M_I)$ transition is needed to calculate the dipole moment of interest here. Since state mixing is negligible, the low- and high-field values of the lifetime are the same. The total lifetimes of the excited substates are all equal. Since the high field effectively decouples \vec{I} and \vec{J} , $\Delta M_I = 0$ for an electronic transition. The $^2P_{1/2}(M_J = +\frac{1}{2}, M_I = \frac{3}{2})$ excited state $|a\rangle$ can then make a transition to the $^2S_{1/2}(M_J = -\frac{1}{2}, M_I = \frac{3}{2})$ ground state $|b\rangle$ or to a third state $|c\rangle$, $^2S_{1/2}(M_J = +\frac{3}{2})$ (see Fig. 9). Neglecting the 6-Å difference in wavelengths of the two transitions

$$\tau_{ac}/\tau_{ab} = |(r_{ab})|^2 / |(r_{ac})|^2 \quad (D6a)$$

$$= \begin{pmatrix} \frac{1}{2} & 1 & \frac{1}{2} \\ -\frac{1}{2} & 1 & -\frac{1}{2} \end{pmatrix}^2 \begin{pmatrix} \frac{1}{2} & 1 & \frac{1}{2} \\ -\frac{1}{2} & 0 & \frac{1}{2} \end{pmatrix}^{-2} = 2, \quad (D6b)$$

where

$$\begin{aligned} & |\langle J' M'_J | r(1, q) | J M_J \rangle|^2 \\ & \propto \begin{pmatrix} J' & 1 & J \\ -M'_J & q & M_J \end{pmatrix}^2 (J' \parallel r(1) \parallel J)^2 \end{aligned}$$

by Edmonds's Eq. (5.4.1).³⁵ Then since

$$\frac{1}{\tau_{ac}} + \frac{1}{\tau_{ab}} = \frac{1}{\tau_a} \quad (D7)$$

and $\tau_a = 28$ nsec, we find that $\tau_{ac} = 2\tau_{ab} = 84$ nsec.

From the partial lifetime $\tau_{ab} = 42$ nsec, one finds

the dipole moment $p_0 = 6.16 \times 10^{-18}$ esu cm from Eq. (36.22) of Ref. 32:

$$\frac{1}{\tau_{ab}} = \frac{4e^2\omega_0^3}{3\hbar c^3} |(\vec{r})_{ab}|^2 = \frac{4\omega_0^3 p_0^2}{3\hbar c^3} \quad (D8)$$

- ¹H. M. Gibbs and R. E. Slusher, Phys. Rev. Letters **24**, 638 (1970).
- ²(a) S. L. McCall and E. L. Hahn, Phys. Rev. Letters **18**, 908 (1967); (b) Phys. Rev. **183**, 457 (1969); (c) Phys. Rev. A **2**, 861 (1970).
- ³C. K. N. Patel and R. E. Slusher, Phys. Rev. Letters **19**, 1019 (1967).
- ⁴C. K. N. Patel, Phys. Rev. A **1**, 979 (1970).
- ⁵F. A. Hopf, C. K. Rhodes, and A. Szoke, Phys. Rev. B **1**, 2833 (1970).
- ⁶P. K. Cheo and C. H. Wang, Phys. Rev. A **1**, 225 (1970).
- ⁷D. J. Bradley, G. M. Gale, and P. D. Smith, Nature **225**, 719 (1970).
- ⁸N. S. Shiren, Phys. Rev. Letters **15**, 341 (1965); Phys. Rev. B **2**, 2471 (1970).
- ⁹L. Davidovich and J. H. Eberly, Bull. Am. Phys. Soc. **15**, 506 (1970); Opt. Commun. **3**, 32 (1971).
- ¹⁰(a) F. A. Hopf and M. O. Scully, Phys. Rev. B **1**, 50 (1970); (b) Phys. Rev. **179**, 399 (1969).
- ¹¹L. E. Estes, D. C. Eteson, and L. M. Narducci, IEEE J. Quantum Electron. **QE-6**, 546 (1970).
- ¹²D. Grischkowsky, Phys. Rev. Letters **24**, 866 (1970).
- ¹³R. L. Byer, W. E. Bell, E. Hodges, and A. L. Bloom, J. Opt. Soc. Am. **55**, 1598 (1965).
- ¹⁴J. P. Goldsborough and A. L. Bloom, IEEE J. Quantum Electron. **QE-5**, 459 (1969).
- ¹⁵Y. V. Troitskii and N. D. Goldina, Opt. i Spektroskopiya **25**, 462 (1968) [Opt. Spectry. **25**, 255 (1968)].
- ¹⁶P. W. Smith, M. V. Schneider, and H.G. Danielmeyer, Bell System Tech. J. **48**, 1405 (1969).
- ¹⁷The authors are grateful to M. V. Schneider for the preparation of the Nichrome film.
- ¹⁸S. P. Davis, Appl. Opt. **2**, 727 (1963).
- ¹⁹H. Walther and J. L. Hall, Appl. Phys. Letters **17**, 239 (1970).
- ²⁰G. L. Lamb, Jr., Rev. Mod. Phys. (to be published).
- ²¹N. F. Ramsey, *Molecular Beams* (Oxford U.P., Oxford, England, 1956), p. 78.
- ²²The $^2S_{1/2}$ energies are given by B. Bederson and V. Jaccarino, Phys. Rev. **87**, 228 (1952), and 2P energies by B. Senitzky and I. I. Rabi, *ibid.* **103**, 315 (1956).
- ²³With a Vidar 520 integrating digital voltmeter.
- ²⁴It was verified many times at low input intensity that there was no delay between right- and left-circularly polarized light. Group-velocity calculations such as those in L. Casperson and A. Yariv, Phys. Rev. Letters **26**, 293 (1971) and D. H. Close, Phys. Rev. **153**, 360 (1967)

since $|\langle J' = \frac{1}{2}, M' = \frac{1}{2} | \vec{r} | J = \frac{1}{2}, M = -\frac{1}{2} \rangle| = |\langle J' = \frac{1}{2}, M' = \frac{1}{2} | r(1, 1) | J = \frac{1}{2}, M = -\frac{1}{2} \rangle| = p_0/e$.^{35,36} The dipole moment to be substituted into the theory using the notation of McCall and Hahn is then $p = p_{MH} = p_0/\sqrt{2} = 4.35 \times 10^{-18}$ esu cm.

yield $-c/\text{const}$, where c is the velocity of light in vacuum and the const is about 100. For much smaller values of absorption the classical group velocity is larger than c , so linear dispersion would advance rather than delay the pulse.

²⁵This effect is similar to optical nutations, but the latter require for their theoretical explanation only the coherent driving of atomic dipoles by an external field. A simultaneous solution of coupled Maxwell and Schrödinger equations is not needed because the absorbers are too scarce to appreciably affect the field. For more about optical nutations see G. B. Hocker and C. L. Tang, Phys. Rev. **184**, 356 (1969).

²⁶H. Kogelnik, Bell System Tech. J. **44**, 455 (1965).

²⁷J. C. Diels, Phys. Letters **31A**, 111 (1970).

²⁸H. M. Gibbs and R. E. Slusher, Appl. Phys. Letters **18**, 505 (1971).

²⁹B. R. Mollow and M. M. Miller, Ann. Phys. (N.Y.) **52**, 464 (1969).

³⁰For example, A. M. Zarem, F. R. Marshall, and F. L. Poole, Elec. Eng. **68**, 282 (1949).

³¹For example, B. H. Billings, J. Opt. Soc. Am. **39**, 797 (1949).

³²L. I. Schiff, *Quantum Mechanics*, 2nd ed. (McGraw-Hill, New York, 1955), p. 253, Eq. (35.21).

³³A. C. G. Mitchell and M. W. Zemansky, *Resonance Radiation and Excited Atoms* (Cambridge U.P., Cambridge, England, 1961).

³⁴J. K. Link, J. Opt. Soc. Am. **56**, 1195 (1966). Other measurements are given in E. L. Altman and S. A. Kazantsev, Opt. i Spektroskopiya **28**, 805 (1969) [Opt. Spectry. **28**, 432 (1969)].

³⁵A. R. Edmonds, *Angular Momentum in Quantum Mechanics* (Princeton U.P., Princeton, N. J., 1957).

³⁶If Eq. (D8) is substituted into Eq. (D5), one has $\alpha = 3Cn_b/\tau_{ab}$,

$$C = \frac{1}{\Delta\nu_D} \left(\frac{\ln 2}{\pi} \right)^{1/2} \frac{\lambda^2}{4\pi},$$

compared with $k_0 = Cn/\tau$ in Eq. (35) of Ref. 33 with $g_1 = g_2$. These values of the absorption coefficient are actually in agreement: $n_b = \frac{1}{2}n$ (half of the total ground-state density n is in the $M_J = -\frac{1}{2}$ substate), $\tau_{ab} = 42$ nsec, $\tau = 28$ nsec. But it is incorrect to use $k_0 = Cn/\tau$ taking n as the density of the $M_J = -\frac{1}{2}$ sublevel and τ as the partial lifetime of the upper $M_J = +\frac{1}{2}$ substate against transitions to the $M_J = -\frac{1}{2}$ substate.